RADIATION RESPONSE FROM A NOVEL UO_2 CRYSTAL

THESIS

Stephan A. Varga, MAJ, USA

AFIT-ENP-MS-16-M-084

DEPARTMENT OF THE AIR FORCE
AIR UNIVERSITY

AIR FORCE INSTITUTE OF TECHNOLOGY

Wright-Patterson Air Force Base, Ohio

AFIT-ENP-MS-16-M-084

RADIATION RESPONSE FROM A NOVEL UO_2 CRYSTAL

THESIS

Presented to the Faculty

Department of Engineering Physics

Graduate School of Engineering and Management

Air Force Institute of Technology

Air University

Air Education and Training Command

in Partial Fulfillment of the Requirements for the

Degree of Master of Science

Stephan A. Varga, BS, MS

MAJ, USA

March 2016

AFIT-ENP-MS-16-M-084

RADIATION RESPONSE FROM A NOVEL UO_2 CRYSTAL

THESIS

Stephan A. Varga, BS, MS
MAJ, USA

Committee Membership:

Dr. J.C. Petrosky
Chair

Dr. J.W. McClory
Member

Dr. D.B. Turner
Member

AFIT-ENP-MS-16-M-084

Abstract

The radiation response of a novel, single-crystalline UO_2 sample was analyzed using several types of radiation. The crystal was exposed to alpha, gamma, and neutron radiation under various environmental conditions and the electronic response of the crystal was measured using a pulse shape discrimination algorithm. The distributions of pulse amplitude (V_{max}) and pulse decay times (τ) were used to compare the output.

This research revealed that the crystal radiation response is exceptionally sensitive to surface conditions, specifically humidity, which tends to alter the time dependent currents resulting from the radiation interactions. The pulse τ can be made to be uniquely distributed for a certain set of conditions allowing to discern alpha, background and gamma irradiation, but it cannot be consistently reproduced. The overall $\Delta\tau$ itself was uniform for all radiation sources measured and the decay distributions were statistically different. This suggests that with well controlled environments, τ distributions may be sufficient to identifying a radiation interaction type.

This preliminary research on novel uranium-based detectors indicates that further research into the crystal surface electronic structure is needed if it is possible to separate radiation types, especially neutron interactions. Furthermore, developing a better method for making crystal contacts to ensure bulk conductivity is a priority.

For my Chuckleheads, without whom, this would not be possible.

I couldn't ask for better friends.

Acknowledgements

I would like to express my appreciation to my advisor, Dr. Petrosky, for his wisdom. His insight and patience were invaluable and ensured the rabbit hole didn't get too deep. I would also like to thank my committee for their constant support. I would like to thank the 22nd Chemical Battalion for providing me with unobstructed access to their ^{252}Cf sources.

Lastly I would like to express my utmost appreciation to my wife. She has provided me with amazing support.

Stephan A. Varga

Table of Contents

Page

List of Figures

List of Tables

RADIATION RESPONSE FROM A NOVEL UO_2 CRYSTAL

1. Introduction

1.1 Background

A majority of fast neutron detection has been primarily accomplished by devices that require neutron moderation in order to take advantage of the higher capture cross sections of ^{6}Li, ^{10}B, and ^{3}He at lower energies.

^{3}He is one of the more commonly used materials for thermal neutron detection. Once costing \$100 per liter, ^{3}He is predicted climb to over \$2,100 per liter because of worldwide shortages [1, 2]. ^{3}He can be extracted from natural gas wells, although some estimates indicate a cost of \$21,000 per liter should this method be used [3]. In order to overcome the ^{3}He shortages, researchers are examining other media to detect neutrons.

UO_2 is typically a low-ordered material; at best polycrystalline, consisting of a mixture of U_xO_y stoichiometries including UO_2, U_3O_8, U_4O_9, and U_2O_5. Research at the Air Force Research Laboratory (AFRL) has resulted in the synthesis of higher order UO_2 crystals via the hydrothermal growth process [4]. Due to their crystal quality, long range order and purity, they have strong potential for use as a single crystal, solid-state neutron detector.

1.2 Research Justification

Since the application of hydrothermal growth to UO_2 resulting in single, well-ordered crystals is a novel process, there has been little in the characterization of

single crystal UO_2 outside of the present research. The properties of UO_2 metal, in general, are well documented. Several researchers have claimed to synthesize single-crystal UO_2 produced by various methods. From these few reports [5,6], single crystal UO_2 is expected to be a semiconductor. The use of UO_2 as a semiconductor has been explored in the context of a photovoltaic material and the construction of a primitive rectifying device has been claimed [7]. The use of UO_2 as a neutron radiation detector has yet to be achieved. It is likely the quality of UO_2 in the previous research has been a limiting factor among other requirements related to device development [6].

1.3 Research Objectives

The objective of this research is to study crystalline UO_2 as applied to the detection of fast neutrons with the penultimate goal of characterizing radiation interactions. The research will serve to answer two principle questions:

1. Can neutron radiation be detected within a high order crystal of UO_2?
2. Can the signal from neutron interactions be distinguished from other radiation interactions?

1.4 Problem Statement

The primary focus of this research is the electronic response of the UO_2 crystal when exposed to radiation. It requires analysis of the pulse amplitude (V_{max}) and decay time (τ), and application of theory to determine the cause of the changes to the crystal electronic response.

1.5 Hypothesis

Radiation interacts with matter through a variety of mechanisms. Exposing a single-crystalline UO_2 sample to ionizing radiation will excite charge carriers within the crystal. The flow of these charge charge carriers produces a current which can be measured via probe tips with a bias applied to the crystal. The pulse amplitude and decay time will depend on the type of ionizing radiation to which the crystal is exposed.

1.6 Sponsorship

The research contained in this document is sponsored and funded by the Domestic Nuclear Detection Office (DNDO). The information contained within this document provides a record of the work accomplished in support of their mission.

1.7 Sequence of Presentation

This thesis is separated into five chapters. The first chapter provides an introduction to the UO_2 crystal and pertinent background information. Chapter two presents the associated theory, along with results of literature searches. Chapter three presents the experimental setup and methodology used for crystal irradiation and data processing. Chapter four describes the results of the experiments and provides analysis. Chapter five presents the conclusion and recommendations for future work.

2. Neutron Detector Theory

2.1 Radiation Interactions

Gamma rays interact with matter primarily through three mechanisms: the photoelectric effect, Compton scattering, and pair production. Because of the photon energies later discussed, the primary interaction mechanism of interest in the present research is Compton scattering. A photon is Compton scattered by striking a nearly free atomic electron. The photon imparts some of its energy to the electron and changes direction [8]. Depending on the incident photon energy, the atom can be ionized, resulting in positively charged space-charge and a free electron.

With regards to neutron interactions in UO_2, the primary mechanism of interest is fission. During this process, a neutron is captured by the ^{238}U nucleus. If the binding energy is overcome, the nucleus splits, generating fission fragments. These fragments are highly ionized and have kinetic energies ranging between 50-110 MeV [8]. In UO_2, these fission fragments will strip electrons from the surrounding material through Coulombic scattering that can be exploited to produce an electric signal.

Alpha particles are heavy charged particles and are generally more energetic than beta particles or gamma rays. Unlike gamma radiation, alpha particles are highly ionized and typically do not undergo angular scattering. Rather, alpha particles undergo a series of Coulombic scattering along a short path (approximately 3 cm in air) similar to fission fragments. At the end of the path, the particles quickly deposit their energy into the surrounding medium. Because of this, alpha particles can resemble fission events, acting as low energy fission fragment surrogates. An overview of radiation interactions in UO_2 is illustrated in Figure 1.

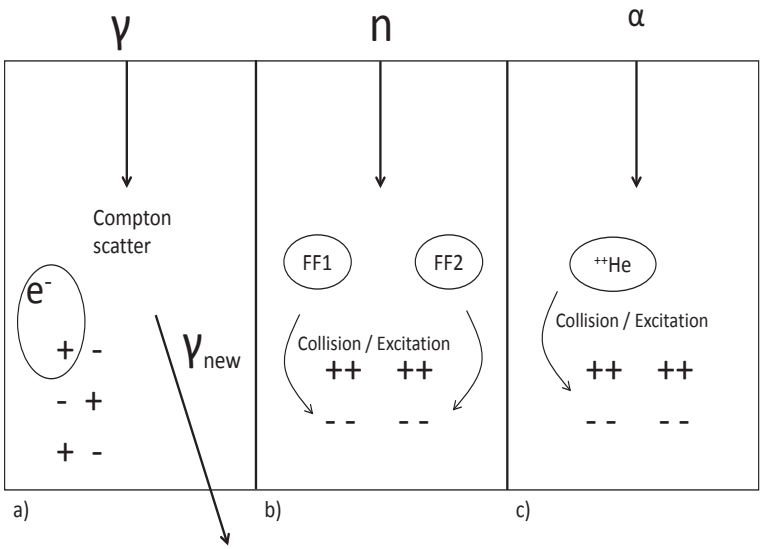

Figure 1. (a) Compton scattering: an electron is excited but can quickly recombine within the crystal. (b) Fission: fission fragments collide with the surrounding medium and excite electrons from the valence band into the conduction band. (c) Alpha bombardment: the alpha particle collides with the medium and excites electrons in a manner similar to fission. Generally, there are overall fewer collisions because alpha particles have much less energy than fission fragments.

2.2 Neutron Detector Materials

Neutrons are generally classified by their energies. The neutron speed (ν) can be calculated with the relationship in (1).

$$\begin{aligned} \sqrt{\frac{2E}{m}} &= v \\ E = &\text{ neutron energy in J} \\ m = &\text{ neutron mass } (1.675 \times 10^{-27}\text{kg}) \end{aligned} \tag{1}$$

Table 1 categorizes neutrons by their associated energies and velocities.

Table 1. Summary of neutron energy categories and velocities. The velocities are associated with the upper energy limit. Data obtained from [9].

Energy Classification	Energy [eV]	Velocity [m/s]
Thermal	0.025	2.18×10^3
Epithermal	0.025–0.4	8.75×10^3
Cadmium	0.4–0.6	1.07×10^4
Epicadmium	0.6 –1	1.38×10^4
Slow	1–10	4.37×10^4
Resonance	10–300	2.4×10^5
Intermediate	300–1×10^6	1.38×10^7
Fast	$>1 \times 10^6$	$>1.38 \times 10^7$

Because they lack charge, neutrons are not measured directly. Rather, they are detected by measuring the by-product of a nuclear reaction. Most neutron detection involves an indirect conversion process where the neutron must first be moderated to thermal energies. The primary reason for the conversion process is mainly due to elements having a large thermal neutron capture cross section that leads to a charged particle emission. The capture cross sections for several prominent detection elements are plotted in Figure 2.

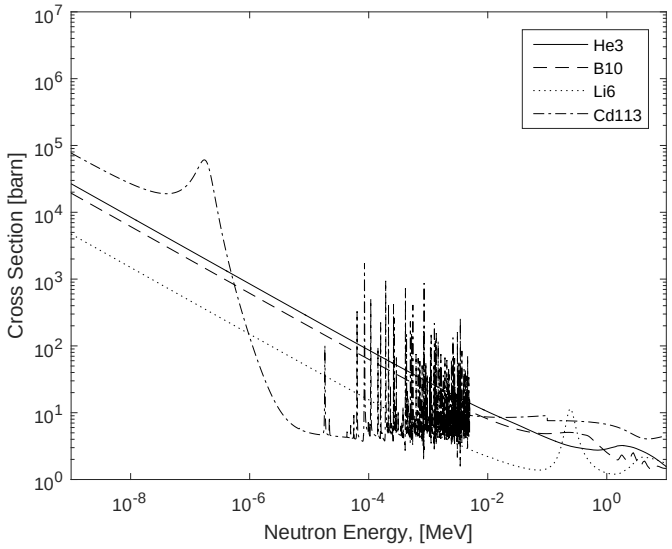

Figure 2. Total neutron cross sections for common materials used in neutron detection. Data obtained from [10].

The thermal neutron cross sections range anywhere from 3–6 orders of magnitude larger than the fast neutron cross sections. The large thermal cross section of these elements make them ideal for neutron detection but require neutron moderation before an interaction can be efficiently detected. The capture reactions from the elements shown in Figure 2 are summarized in Table 2. It is the interaction, usually through ionization, of the secondary particles within the detection medium that is used to detect incident neutrons.

Table 2. Neutron reactions used in common detector materials. Data obtained from [11].

^{3}He	+	n	→	^{3}H	+	p	+	764 keV
^{6}Li	+	n	→	^{3}H	+	α	+	4.78 MeV
^{10}B	+	n	→	^{7}Li	+	α	+	2.31 or 2.79 MeV
^{113}Cd	+	n	→	^{114}Cd	+	γ	+	9.042 MeV

Regardless of the material used, all neutron detectors share the same general characteristics:

- Efficiency: Because uncharged radiation (neutrons and photons) must have an interaction and conversion process before it can be detected, there is some probability that no interaction occurs, leading to loss. The higher the efficiency, the better the detector is at registering events.

- Gamma-neutron separation: Gamma-neutron separation refers to the pulse output of the detector. The pulse outputs from neutron and photon interactions differ primarily in their pulse decay. If the pulses overlap, it is not possible to differentiate a photon from a neutron. Because of this, neutron detectors must be able to discriminate incident gamma events from neutron interactions.

- Commercial availability: ^{3}He is the gas of choice for thermal neutron detection, largely because of its capture cross section (Figure 2) as well as a nearly perfect discrimination of the neutron from gamma signals [12]. ^{3}He, however, is also in global short supply [1, 2, 13]. Both ^{6}Li and ^{10}B have large thermal neutron capture cross sections. Their natural abundances, however, are $\sim 8.5\%$ and 20% respectively. These isotopes must be further enriched before they are used in neutron detectors [11].

2.3 Neutron Detector Technologies

A resistive detector is a very basic type of radiation detector. In a resistive detector, a voltage is placed across a medium. The medium is then exposed to radiation. Measurements are made based on changes in resistance due to changes in the majority charge carrier population.

A resistive detector relies on changes to the material's majority carrier population; while this is structurally simplistic, it suffers from low sensitivity. A variety of other methods can be employed. These technologies can be broken down into four general categories: scintillators, proportional counters, ionization chambers, and semiconductor diodes.

Scintillation Detectors

Scintillation detectors operate by amplifying a light response from the interaction of the scintillation material and secondary particles. Neutrons pass through a conversion material which results in secondary particles. The scintillation material is ionized through collisions with these particles. Scintillation detectors include a variety of material, including organic, crystal, plastic, and glass materials. Organic scintillators are favored for fast neutron detection because of their higher hydrogen content.

The increased hydrogen content maximizes elastic collisions between the neutron and hydrogen nucleus. Like gamma scintillators, these devices must efficiently collect and amplify the light. This is accomplished via a photomultiplier tube. These tubes also require high-voltage power supplies.

Although significant technological advances have been made in the field of scintillation neutron detectors, a common shortcoming of these detectors is they tend to have poor neutron-gamma separation and require further pulse shape discrimination in order to separate events [12, 14].

Proportional Counters

Proportional counters use a gas to amplify charge (ions) from the charged particles generated by a neutron absorption reaction in the conversion material. Unlike gamma detectors, the conversion material and the gas are usually the same. Most of the current proportional counters use BF_3 as the detection medium [11, 13]. Typical BF_3 tubes are enriched in ^{10}B resulting in greater efficiency than those containing naturally occurring boron (20% ^{10}B–80% ^{11}B). The tubes are usually constructed from aluminum and the gas is under low pressure. Pulses are formed by the resulting $^{10}B(n,\alpha)^7Li$ reaction. The ^{10}B absorbs a neutron, generating an alpha particle and a recoil ^7Li nucleus which travel in opposite directions. The movement of these two particles generates ion pairs in the BF_3 gas which are subsequently measured.

Ionization Chambers

Similar to proportional counters, ionization chambers are devices that measure the charge obtained from ionizing radiation. The difference between proportional counters and ionization chambers is largely based on the amount of voltage applied and location of the conversion element. In both, a potential is applied between two

electrodes creating an electric field. The chamber is then filled with a gas. When the gas is ionized, the resulting ion-pairs move under influence of the electric field and are collected on an anode and cathode. In the case of ionization chambers for neutron detection, the chamber is usually lined with a ^{10}B compound. Ion pairs are produced from the interactions of the products of the ^{10}B(n,α)^{7}Li reaction.

One ionization chamber of specific interest is the fission chamber. The walls of a fission chamber are lined with enriched ^{235}U and the chamber is filled with a choice gas, typically argon. Following a fission event, the fission fragments will ionize the gas, which is detected. Because fission chambers are constructed with fissionable materials they have an irreducible alpha background. However, since fission is much more energetic than an alpha particle, the background pulses can be discriminated based on pulse amplitude [11].

Fission chambers are more commonly used in reactor instrumentation with normal operating fluxes of 5×10^{13} n cm^{-2} s^{-1} [11, 15]. These neutron fluxes are orders of magnitude higher than those experienced by neutron detectors in normal environments. Fission chambers can operate in these high fluxes because of their overall inefficiency; outputs from an efficient neutron detector under high-flux environments would result in signal pile up. Fission chambers also do not efficiently detect fast neutrons but rely on moderation from the surrounding chamber material, typically aluminum.

Semiconductor Diode Neutron Detectors

Semiconductor diode neutron devices have been investigated extensively for several decades. They are gaining in interest, largely due to their fast response to charge carriers, size, and low power requirements. Charge carriers in semiconductors are conduction electrons and holes. Semiconductors are generally categorized as p-type

(increased hole concentration) or n-type (increased electron concentration). Most semiconductor devices operate on the principle of a p-n junction. The p-n junction is a boundary between two types of semiconductors and is the site where the electronic action of the device takes place [16]. Si-based detectors have been of particular interest because of their high electron and hole mobilities ($\sim 1,500$ and ~ 500 cm^2/V respectively) [11, 17]. The mobility characterizes how quickly an electron (or hole) can move through the material under an applied electrical field. A Si-based neutron device requires a conversion layer in order to detect the neutron because the neutron does not ionize. These layers typically include those elements with high capture cross sections, ^{6}Li, ^{10}B, and ^{155}Gd, for interactions that emit charged particles.

Recent advances in semiconductor neutron detectors include adding microstructured patterns to the semiconductor and then back-filling with a neutron-reactive species such as ^{6}Li and ^{10}B [18]. High purity germanium (HPGe), a common gamma solid-state detector, is being investigated to evaluate fast neutrons by monitoring the 596 and 691 keV deexcitation gamma resulting from inelastic scattering from within the Ge crystal [14]. Other semiconductor materials such as CdZnTe and GaAs are being investigated as well. Regardless of the semiconductor, these devices still rely on some conversion/moderation mechanism.

2.4 Fission Overview

Natural uranium contains concentrations of both ^{235}U (0.7%) and ^{238}U (99.3%). ^{238}U is not a fissile material, that is, it is unable to sustain a fission chain reaction. However, given the correct neutron threshold energy greater than 1 MeV, ^{238}U can undergo fission. Its average microscopic fission cross section for fast neutrons is approximately 0.415 barns [19]. While this value may appear small, the fact that ^{238}U has a fast fission cross section is somewhat unique. Most lighter-Z elements,

such as those used in neutron detection, have negligible fast fission cross sections at 1 MeV. The neutron cross sections for both ^{235}U and ^{238}U are compared in Figure 3.

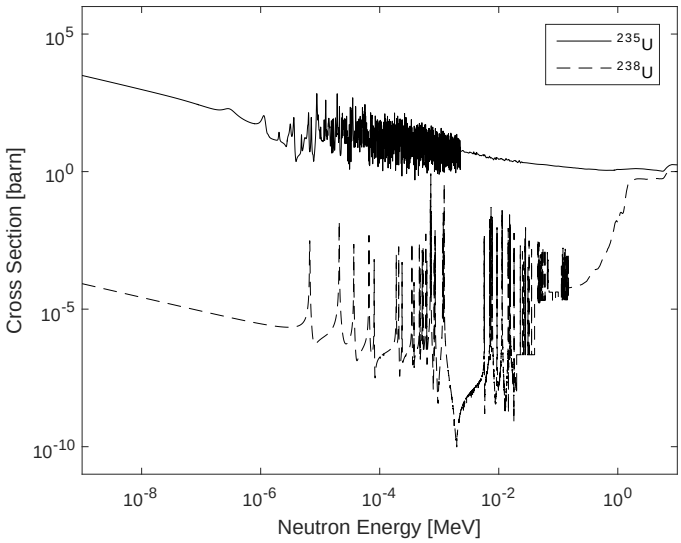

Figure 3. Neutron fission cross section for ^{235}U and ^{238}U. ^{238}U fission cross section becomes non-negligible for neutron energies above 1 MeV. Data obtained from [10].

2.5 Neutron Sources

Neutron Generators

Neutron generators use linear accelerators that fuse hydrogen isotopes together to produce neutrons. The two most common reactions involve fusing two atoms of deuterium (D-D) or fusing deuterium with tritium (D-T). One of the atoms is ionized and then accelerated into a hydride target loaded with deuterium or tritium. Fusion between ionized atoms and the target causes neutrons to be isotropically released. Neutron fluxes vary between generator model and reaction used, but are generally between 10^7–10^{10} n s^{-1}. The primary difference between the two fusion reactions is the neutron energy. D-D reactions produce 2.5 MeV neutrons while D-T reactions produce 14.1 MeV neutrons. Neutron generator reactions are summarized in Table 3.

Table 3. Neutron reactions in neutron generators. The D-T reaction always produces a 14.1 MeV neutron; the D-D reaction will produce a 2.5 MeV neutron 50% of the time.

Reaction							Neutron Energy [MeV]
D	+	T	→	n	+	α	14.1
D	+	D	→	n	+	^{3}He	2.5
				^{3}H	+	p	–

Spontaneous Fission

Spontaneous fission is a form of radioactive decay. The process of spontaneous fission is similar to that of neutron-induced fission except no neutron capture is required. Spontaneous fission is almost exclusively limited to the heavier, and therefore synthesized, actinides such as Pu, Cm, and Cf. An overview of spontaneous fission elements is presented in Table 4.

Table 4. Overview of spontaneous fission for select elements. Of all elements which spontaneously fission, ^{252}Cf produces the largest number of neutrons per fission, as well as the highest flux. Table reproduced from [20].

Nuclide	Half-life	Fission probability per decay	Neutrons per fission	Neutrons per gram-second
^{235}U	7.04×10^8	2.0×10^{-9}	1.86	3.0×10^{-4}
^{238}U	4.47×10^9	5.4×10^{-7}	2.07	1.36×10^{-2}
^{239}Pu	2.31×10^4	4.4×10^{12}	2.16	2.2×10^{-2}
^{240}Pu	6.57×10^3	6.50×10^{-7}	2.21	9.2×10^2
^{250}Cm	6.9×10^3	6.1×10^{-1}	3.31	1.6×10^{10}
^{252}Cf	2.64×10^3	3.09×10^{-2}	3.73	2.3×10^{12}

Beryllium sources

Beryllium sources are commonly used in laboratories for neutron production. The stable isotope of beryllium, ^{9}Be, has a loosely bound neutron which requires 1.7 MeV to be released from the nucleus. Beryllium will emit this neutron when coupled to a reaction whose Q-value exceeds 1.7 MeV. Two common coupled reactions are the

α-Be and γ-Be reaction. If ^{9}Be is coupled with an average alpha decay (4-6 MeV), the following reaction occurs:

$$\alpha + {}^{9}Be \rightarrow {}^{12}C + n. \tag{2}$$

α-Be sources are generally used by mixing a long-lived alpha-emitter such as ^{239}Pu or ^{241}Am to the ^{9}Be. These sources generally produce 10^{7} n (s Ci)$^{-1}$ [11] with neutron energies ranging between 0.1–10 MeV. ^{9}Be can also be coupled to gamma emissions to produce neutrons. The process, called photoneutron production, is similar to that of the α-^{9}Be reaction in (2):

$$\gamma + {}^{9}Be \rightarrow {}^{8}Be + n. \tag{3}$$

A photon must be energetic enough to release a neutron in (3). Because of this constraint, ^{24}Na (which emits a 2.76 MeV gamma) is a common isotope used in this reaction. An advantage of photoneutron production is the resulting neutron spectrum is more monoenergetic than that produced by α-^{9}Be sources. Photoneutron production yields similar production rates of α-^{9}Be neutron production [11].

2.6 UO_2 as a Semiconductor

The properties of UO_2 metal, in general, are well documented. The article by Meek [5] is the first known reference to the use of uranium oxides, particularly UO_2, as an semiconductor. The use of UO_2 as a semiconductor has been explored in the context of a photovoltaic material and primitive rectifying device construction has been claimed [7]. From these few reports, single crystal UO_2 is expected to perform as a semiconductor, although its band gap and intrinsic carrier types are not yet known.

2.7 Semiconductor Overview

Figure 4 diagrams the relationship of the band gap energy for a generic conductor, insulator, and semiconductor. Conductors share an overlap between the conduction and valence bands. This allows electrons to move freely within the material. For insulators, the gap between the conduction and valence band is sufficiently large, on the order of 5 eV, so that electrons generally remain in the valence band at room temperature. In semiconductors, the band gap is less than in insulators but does not overlap (as in conductors) such that the probability of thermal excitation is dependent on the size of the band gap.

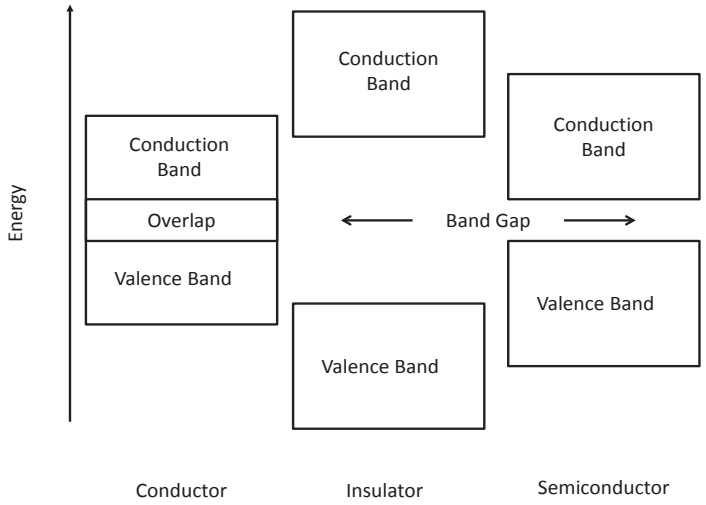

Figure 4. Overview of band gaps in semiconductors, conductors, and insulators.

The excitation process creates an electron in the conduction band but also leaves a vacancy (hole) in the valence band. The electron-hole pair is analogous to ion-pairs in gases. As previously alluded to, thermal excitations contribute to all nonzero temperature crystals. The probability of thermal excitation is calculated using (4) [11].

$$p(T) = CT^{\frac{3}{2}}\, \mathrm{e}^{-\frac{E_g}{2kT}} \tag{4}$$

$E_g =$ bandgap energy

$k =$ Boltzmann constant

$C =$ proportionality constant characteristic of the material

In order to mitigate the thermal generation of charge carriers in semiconductors with very small band gaps (such as Ge), they are usually cooled with liquid nitrogen. Single crystal UO_2, however, is expected to have has a much larger band gap of around 1.3 eV [21] and like Si, will not require cooling.

Pulse Formation and Charge Collection

When a neutron fissions a ^{238}U atom, approximately 165 MeV of energy is released in the form of fission fragments [19]. These fragments are highly ionized and have a large amount of kinetic energy. Fission fragments interact with surrounding electrons via Coulombic interactions. The kinetic energy combined with the Coulombic interactions result in multiple ionization events which excite electrons into the conduction band of the crystal. The electrons and holes will move in the periodic potential of the crystal under the influence of an applied electric field. The holes will move toward the negative potential, the electrons toward the positive potential. It is the collection of these carriers through contacts placed on the material that provides a means of detecting the ionization event. When collected with a charge sensitive amplifier, the phenomenon leads to the production of a detection 'pulse'.

Figure 5 presents the results of a TCAD simulation of a neutron interaction with a simulated UO_2 crystal. The simulation included charge formation due to interactions of the fission fragments (in time) along with the time for the charge to migrate to a contact, placed approximately 4 μm from the event. The simulation did not include actual values for the UO_2 (which have not yet been measured) but notionalized the device using mobility and lifetimes from Si. The figure indicates that a very sharp, distinguishable pulse can be potentially created in UO_2 that performs similar to Si [22].

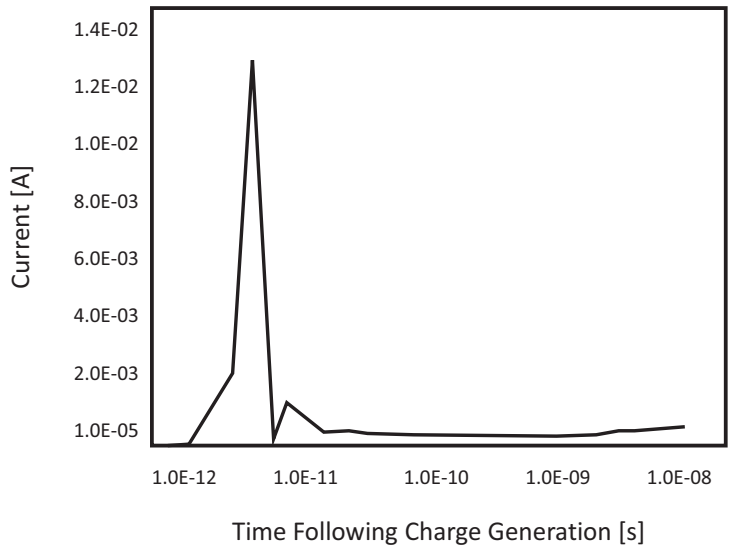

Figure 5. Plot showing simulated charge collection resulting in a pulse. Reproduced from [22].

Pulse formation is entirely dependent on collection of charge carriers. While the formation of charge carriers relies on ionization events, their collection is influenced by several factors, including the electric field strength, carrier mobility, and carrier lifetime. Table 5 compares carrier mobilities and band gaps for known semiconductors and UO_2. Table 5 highlights the fact that these parameters have not been adequately reported for UO_2 and further research is needed to illuminate this topic.

Table 5. Properties of select semiconductors. In comparison to other semiconductors, the values for UO_2 are either estimates or based off of hyperstoichiometric UO_2 samples. Values for single crystalline UO_2 are currently unreported [11, 16, 23].

Semiconductor	Band Gap [eV]	Electron Mobility (cm^2/V)	Hole Mobility (cm^2/V)
Ge	0.66	3,900	1,900
Si	1.12	1,450	500
GaAs	1.42	8,000	400
CdTe	1.56	1,050	100
UO_2	1.3*	-	0.0015*
*Estimated			

Carrier lifetime is largely a function of crystal impurities. In an ideal semiconductor detector, all of the charge carriers created would be collected. Carrier trapping and recombination sites can significantly reduce charge collection. In most semiconductor radiation detectors, the charge collection time is very short (10^{-8}–10^{-7} s) while the lifetime is much longer (10^{-5}–10^{-4} s). This lifetime allows sufficient time for the charge to be collected [11, 16].

The product of carrier lifetime and mobility, commonly referred to as the $\mu\tau$-product, is an indicator of the potential of how well a device will measure radiation. The greater the $\mu\tau$-product, the greater potential a device has as a radiation detector. The $\mu\tau$-product for Si- and Ge-based detectors are well documented [11, 16]. The literature is absent in this regard to UO_2. However, the semiconductor band gap combined with the neutron fission cross section suggests that UO_2 may useful in neutron detection.

2.8 UO_2 as a Neutron Detector

The use of UO_2 as a radiation detector has yet to be achieved. Kruschwitz's report [6] is the first known research on the use of depleted uranium dioxide as a

direct conversion neutron detector. Using arc-fusion grown UO_2 crystals and a ^{252}Cf source, Kruschwitz claimed to have manufactured simple Schottky diodes in which neutron-induced fission could be measured. Kruschwitz also reported on experimental shortcomings including quality of the manufactured Schottky diodes and quality of the UO_2 crystal. In spite of these shortcomings, Kruschwitz concluded that UO_2 crystals proved promising in neutron detection.

Young conducted similar research on a novel single-crystalline UO_2 crystal [24]. Based on qualitative analysis of pulse amplitude (V_{max}) and pulse decay (τ) histograms, Young determined that a primitive device employing mechanical contacts on a single-crystalline UO_2 sample responded differently to both alpha particles and X-rays. This research was similar to that of Kruschwitz in concept. The significant difference between the two experiments was the UO_2 crystal quality. Whereas Kruschwitz experimented on arc-fusion grown crystals, Young experimented on hydrothermally grown crystals. These crystals are inherently of greater quality. Because of the growth process, Young's UO_2 crystal sample was significantly smaller. Kruschwitz's samples were on average 0.5" in diameter and 1.0–1.5 mm thick [6]. Young's sample was approximately 1 mm^3. In spite of the small sample, Young determined the signal from such a primitive device was inherently noisy but had promise as a detector.

3. Methodology

3.1 General

In order to determine whether or not the crystal could be used to detect fast neutrons, the crystal and the electronics had to be characterized. System characterization included measuring system responses from the preamplifier and background. After the system was characterized, the crystal was exposed to alpha, gamma, and neutron radiation. Alpha particles served as fission fragment surrogates while gammas were used to observe radiation differentiation.

Exposure times varied; each pulse generated a file saved to the oscilloscope buffer. Pulses were collected until the buffer was full. Generally, background measurements took longer to collect than radiation measurements. Signals from the oscilloscope were post-processed and analyzed using an in-house analysis code. An overview of the process is illustrated in Figure 6.

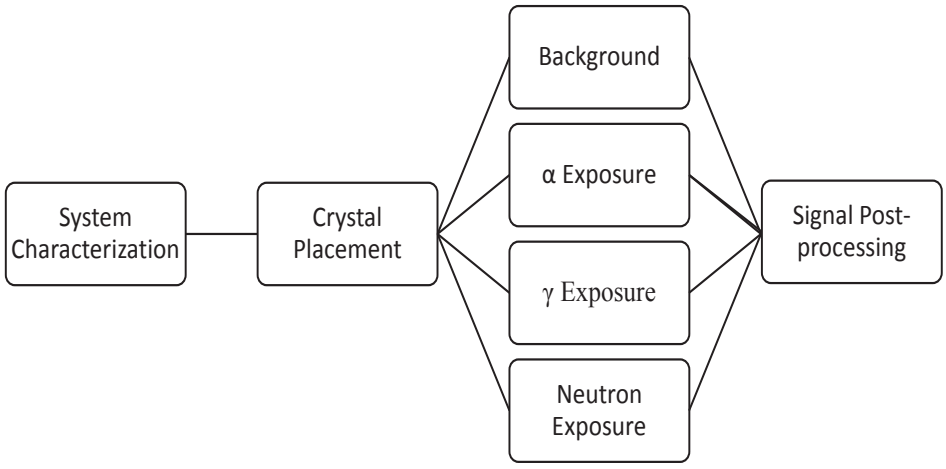

Figure 6. Experimental overview: the system electronics were first characterized. Once the crystal was placed in the probe station, the crystal was irradiated. The data was processed using an in-house algorithm.

3.2 System Characterization

In order to properly capture pulses, the electronics were characterized. A pulser was connected to an ORTEC 142PC preamplifier in order to determine the pulse decay time. The pulse decay time was measured using a Tektronix DPO 7100 oscilloscope and was determined to be 144 μs. This decay time represented the ideal response from the preamplifier and was the decay time used to trigger events in the oscilloscope.

3.3 Oscilloscope Settings

In order to capture pulses from the crystal, a variety of trigger options were explored. The trigger setting which best captured pulses was a transition trigger. A transition trigger is initiated on a pulse edge which must first traverse two preset voltage thresholds and decay within a certain time. For all experiments, the thresholds were set to 0.882 and 2.39 V and the decay time was 150 μs. These thresholds were chosen based off of visual inspection of the signals from various radiation sources. The upper threshold was selected to be above the visual noise floor while the lower threshold was calculated using (5).

$$V = V_o \mathrm{e}^{-\frac{t}{\tau}} \tag{5}$$

3.4 Equipment Setup

The crystal was placed in an acrylic probe holder in order to minimize neutron activation products during irradiation. Tungsten probe contacts were placed 180° in order to maximize resistivity and collection volume. Figure 7 is a schematic of the crystal in the probe station.

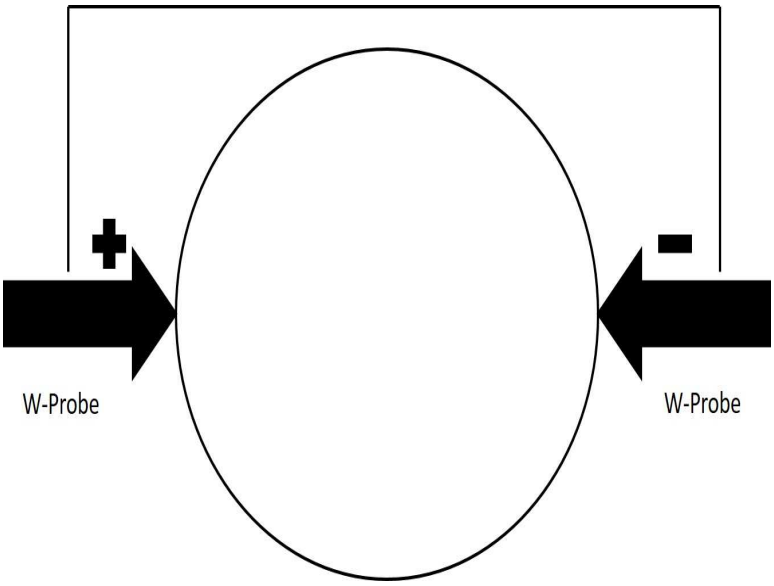

Figure 7. Diagram of the crystal in the probe station used for all experiments.

A potential of 130–150 V was applied to the crystal, which resulted in a potential difference of 4.5–4.7 V across the crystal. The electrical signal was connected to an ORTEC 142PC preamplifier for signal amplification. In early experiments, a recurring 18 kHz signal was observed in the signal. A low-pass filter was applied to remove it. The signal was then processed in an oscilloscope. An overview of the setup is diagrammed in Figure 8.

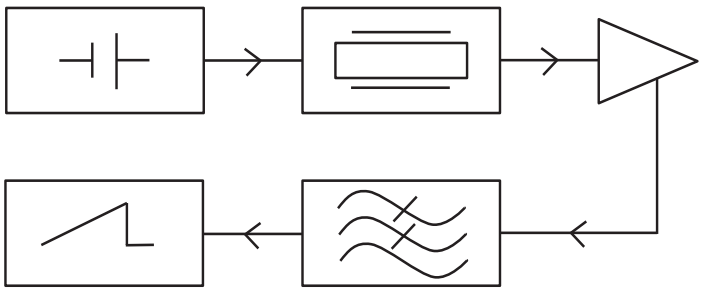

Figure 8. Electronic schematic: a high voltage power supply was connected to the crystal. The signal was sent to a preamplifier, an 18 kHz low-pass filter, and processed on an oscilloscope.

3.5 Alpha Irradiation

^{241}Am has several alpha and low energy gamma decay chains. These decays are illustrated in Figure 9. Because alpha particles are highly ionizing, they transfer their energy in a short distance and have low penetration power.

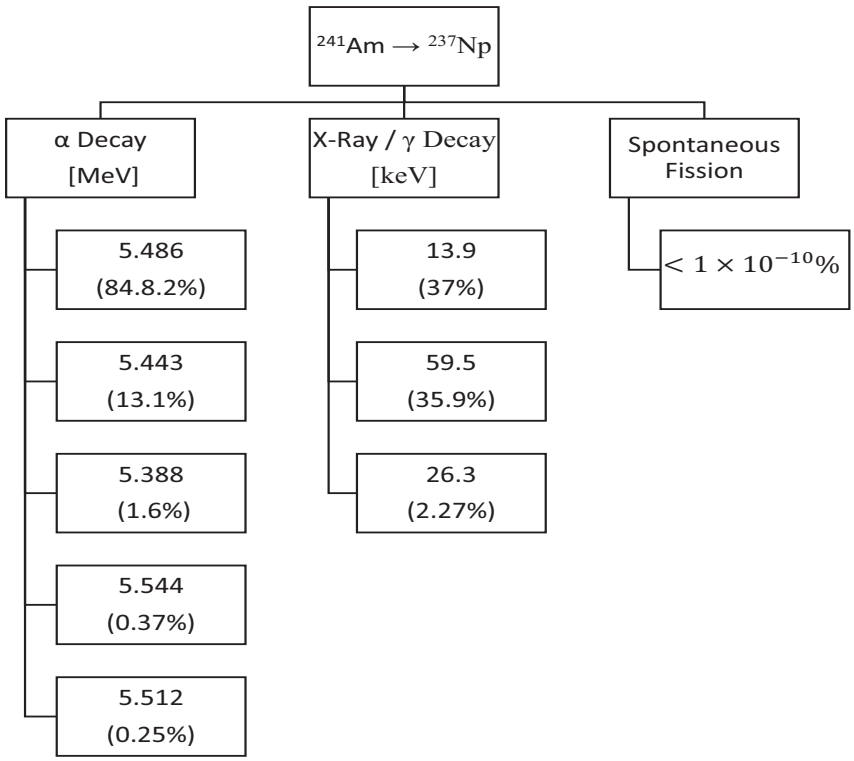

Figure 9. ^{241}Am decay scheme: values in parentheses are the relative intensities. Data obtained from [25].

The stopping power (-dE/dx) for a given material is the average linear rate of energy loss of a heavy charged particle in that material. The range of a heavy charged particle in a material is the distance it travels before coming to rest. Stopping Range of Ions in Matter (SRIM) solves the Bethe-Bloche equation using Monte-Carlo statistics [26] to determine the stopping power of a material and range of a heavy charged particle.

UO_2 stopping power and alpha range were modeled in SRIM using 5.48 MeV alpha particles. This energy was assumed using a weighted average of ^{241}Am alpha

decays. The ^{241}Am sources were standard smoke detector sources. It was assumed that they had $\sim$2 μm gold foil encapsulation. Upon striking a 2 μm gold surface, a 5.48 MeV alpha particle loses approximately 1.4 MeV of kinetic energy. The stopping power of air is much lower, and the energy loss of an alpha particle traveling through 1 mm air is less than 250 keV. Therefore, the alpha particle strikes the surface of the UO_2 crystal with approximately 4.0 MeV kinetic energy, with an estimated range of 8.67 μm. Figures 10a and 10b graph the projected range of ^{241}Am alpha particles and the stopping power of the gold, air, and UO_2 respectively.

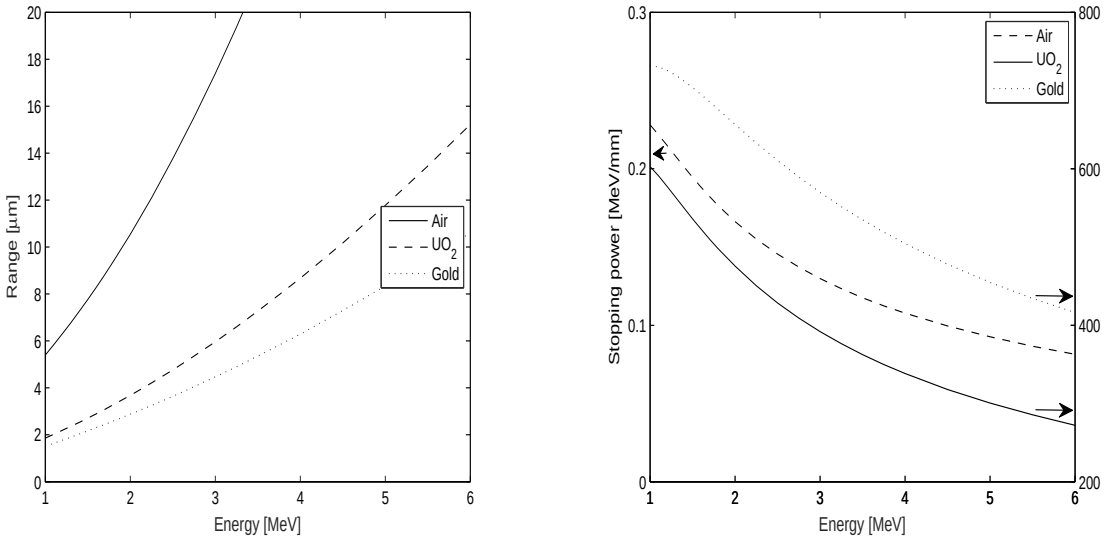

(a) (b)

Figure 10. (a) Plot showing range of an alpha particle in material as a function of energy. Because of material densities, an alpha particle with a given energy will travel much shorter distances in gold or UO_2 than in air. (b) Plot showing stopping power of material (MeV/mm). The stopping power of air (represented by the dashed lines and left y-axis) is considerably less than that for gold or UO_2.

In order to irradiate the crystal with alpha particles, the source was suspended 1 mm over the crystal. Figure 11 illustrates the alpha irradiation setup.

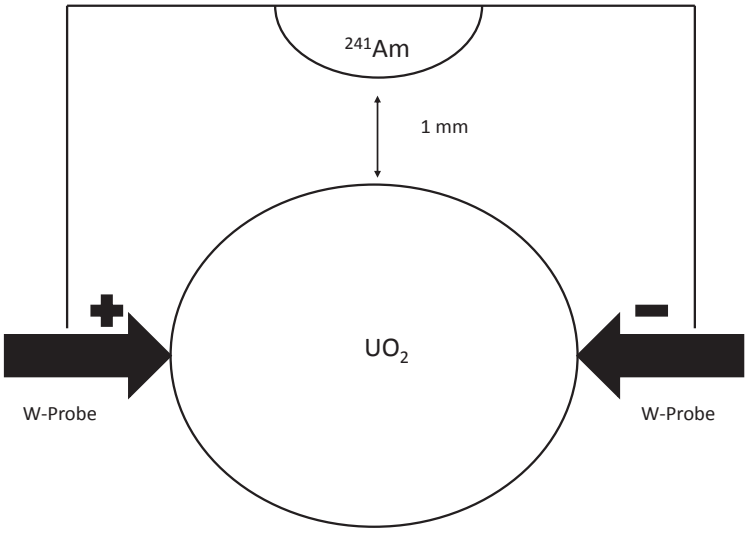

Figure 11. Overview of alpha irradiation: an ^{241}Am source was suspended approximately 1 mm over the crystal.

The crystal was irradiated with alpha particles using a $\sim$ 36,783 Bq ^{241}Am source. This activity was calculated using (6), and an activity of 1 μCi on 31 Aug 2011.

$$\mathscr{A} = \mathscr{A}_o \mathrm{e}^{\frac{\ln 2}{t_{1/2}}} \tag{6}$$

The source was placed directly over the crystal and pulses were recorded on the oscilloscope. Measurements were taken with full source exposure as well as with a 0.45 mm paper shield blocking the alpha source. The purpose of the paper shield was to differentiate between alpha particles and photons from the ^{241}Am source.

3.6 Gamma Irradiation

The crystal was irradiated with two different gamma sources: ^{55}Fe and ^{60}Co. These two sources provide both low and high energy photons respectively. While ^{55}Fe emits Auger electrons and 5.8 keV photons, ^{60}Co emits two photons of 1174 and 1332 keV. The decay of both sources is illustrated in Figure 12. The activities

of the sources were 1.306×10^5 and 1.62×10^6 Bq for ^{60}Co and ^{55}Fe respectively. It was assumed source encapsulation shielded the Auger electrons. Both gamma sources were 2.54 cm from the crystal during gamma irradiation.

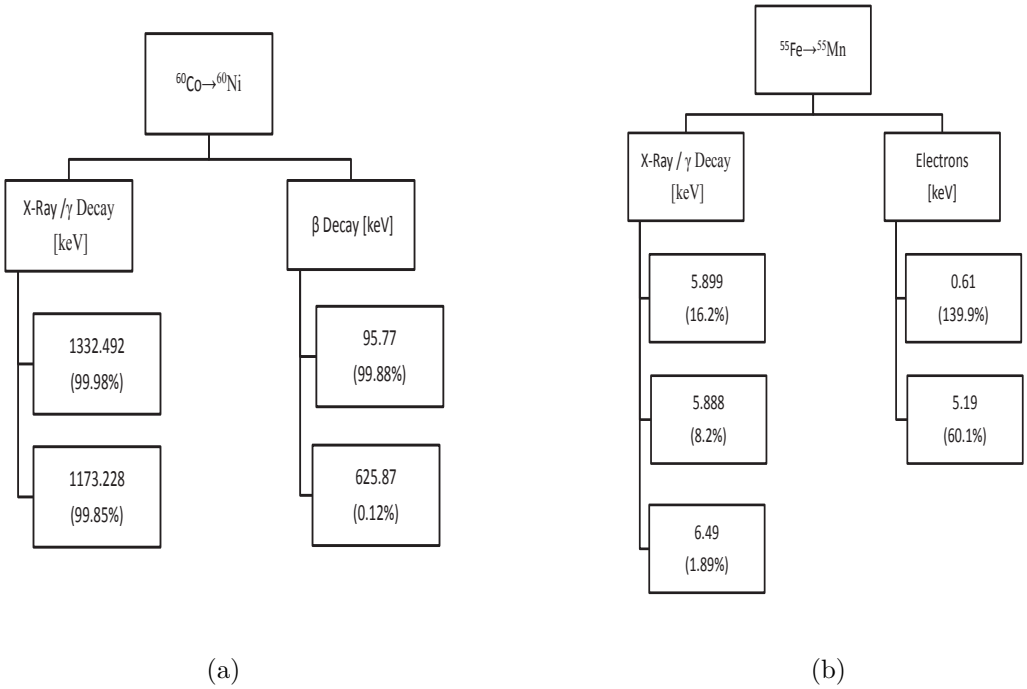

(a) (b)

Figure 12. Decay schemes for (a) ^{60}Co and (b) ^{55}Fe. The values in parentheses are the relative intensities of the decay. Data obtained from [25].

3.7 Neutron Irradiation

^{252}Cf is a widely used laboratory neutron source. Although ^{252}Cf decays primarily by alpha emission, ^{252}Cf has an approximate 3% spontaneous fission rate which produces 3.7 neutrons on average per spontaneous fission, along with an associated gamma spectrum from the fission. The crystal was irradiated with three ^{252}Cf sources with a combined neutron activity of 6.66×10^7 Bq. Figures 13a and 13b represent the decay scheme and gamma spectrum from the spontaneous fission of ^{252}Cf respectively.

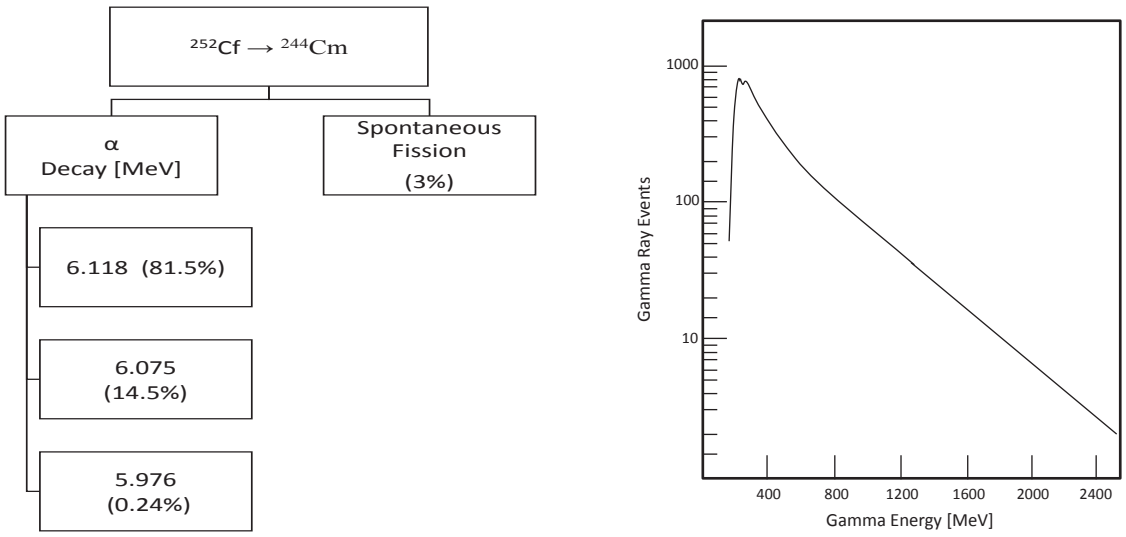

(a) (b)

Figure 13. (a) Decay scheme for ^{252}Cf. The values in parentheses are the relative intensities of the decay. Data obtained from [25]. (b) Gamma spectrum from spontaneous fission of ^{252}Cf. Reproduced from [27].

The sources were suspended approximately 1" over the crystal and the crystal was irradiated. This configuration resulted in a neutron flux of approximately 2.32×10^7 n s^{-1} over the crystal. Figure 14 is a schematic of the neutron irradiation setup.

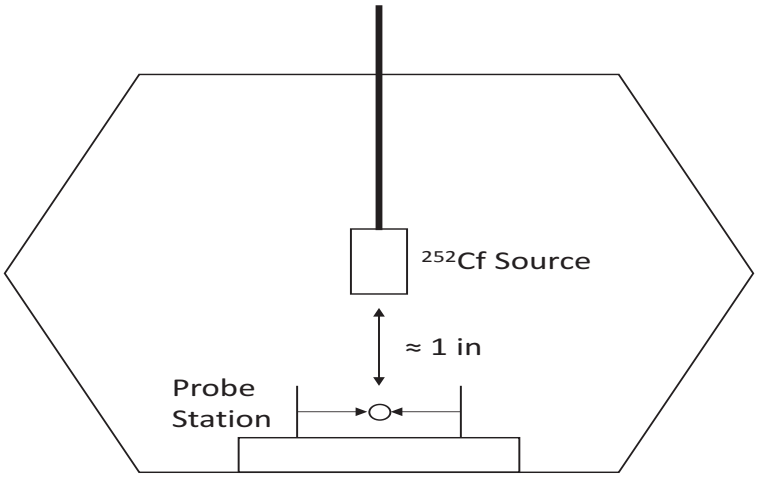

Figure 14. Schematic of neutron irradiations. The ^{252}Cf sources were suspended approximately 1" over the crystal which produced a neutron flux of approximately 2.321×10^7 n s^{-1} over the surface of the crystal.

3.8 Signal Post Processing

Each data set produced $\sim$ 32,000 pulses. Each pulse consisted of time and voltage data. An algorithm was developed in order to analyze the volume of data sets. The pulses were smoothed using an intrinsic Savitsky-Golay smoothing routine. The Savitsky-Golay smoothing routine increases the signal-to-noise ratio by fitting successive sets of low-degree polynomials by the method of linear least squares. This smoothing method is appropriate, as the data points are all equally spaced.
Figure 15 depicts the raw data and the result of the smoothing routine.

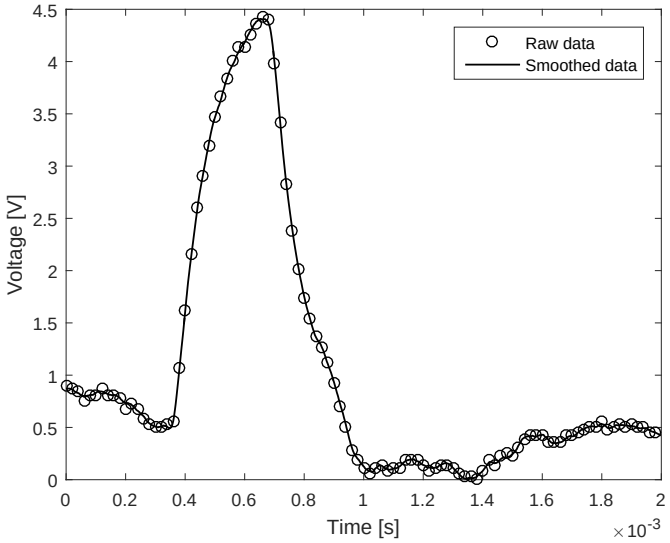

Figure 15. Plot showing raw and smoothed data. Data was smoothed using a Savtisky-Golay smoothing routine.

The τ and V_{max} was analyzed for each pulse by using an algorithm developed by Young [24]. This algorithm executed a curve fitting routine along the curve of the pulse fall time. Each pulse was contained in a fitting window. The end of the pulse was assumed when the derivative of the pulse, (7), crossed zero within the fitting window. A curve was then fit to (5). The coefficients returned from the fitting routine were τ and V_{max}.

$$\frac{\mathrm{d}v}{\mathrm{d}t} = -\frac{1}{\tau} V_o \mathrm{e}^{-\frac{t}{\tau}} \tag{7}$$

An overview of the fitting algorithm applied to a pulse is illustrated in Figure 16.

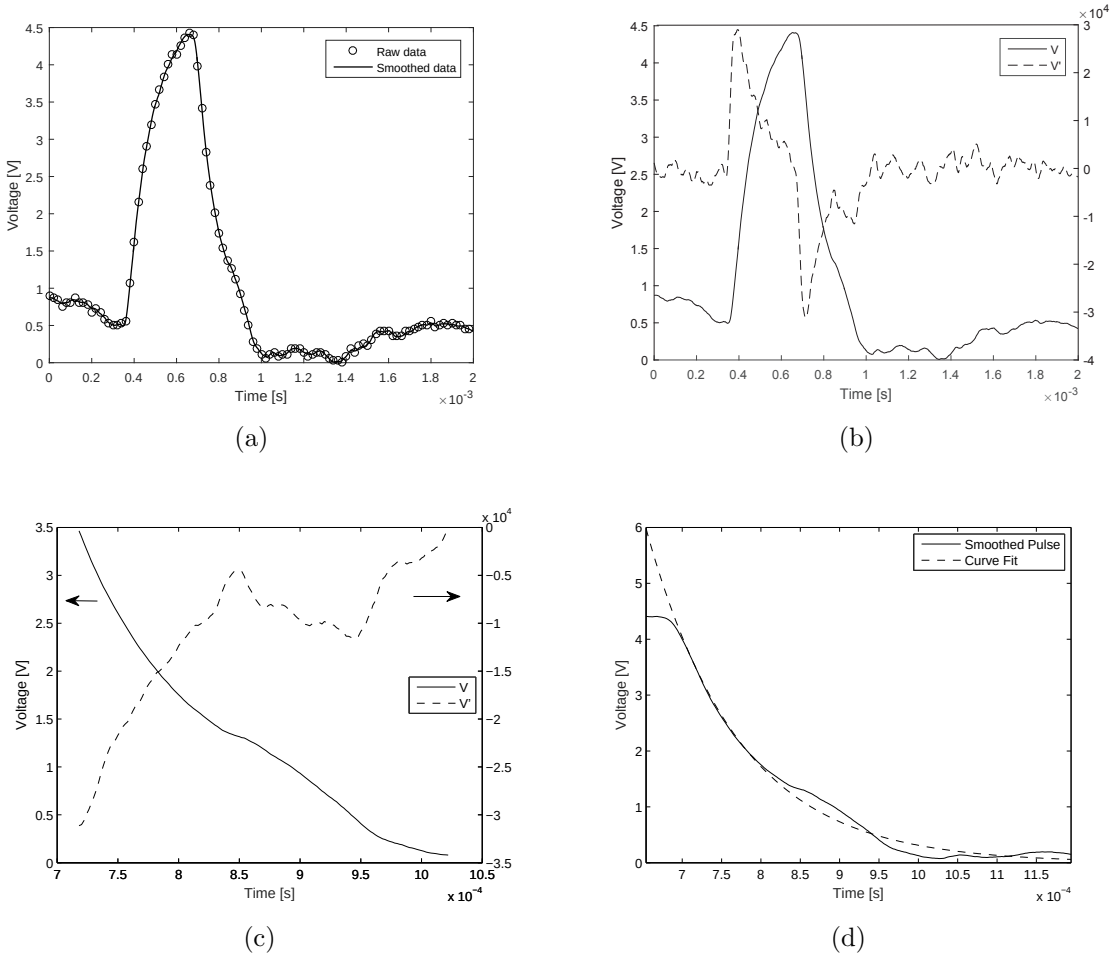

Figure 16. (a) The pulse was first smoothed. (b) The derivative of the pulse (V') was determined in order to find the end of the pulse. The end of the pulse was assumed when the derivative was zero. (c) A fitting window was established from the trigger point to the end of the pulse. (d) A curve was fit to the data points within the window.

3.9 Algorithm Improvement

In order to test the validity of the original algorithm developed by Young, 200 pulses each from two separate background data sets were manually analyzed. Pulses

were selected by visual inspection; only valid pulses were selected. Clipped pulses or pulses with no defined rise time were not analyzed. Raw data was smoothed and the pulse maximum was manually obtained. Of the 200 pulses, 94 were selected for analysis from the first data set; 99 were selected from the second. Figure 17 represents an example of a valid pulse.

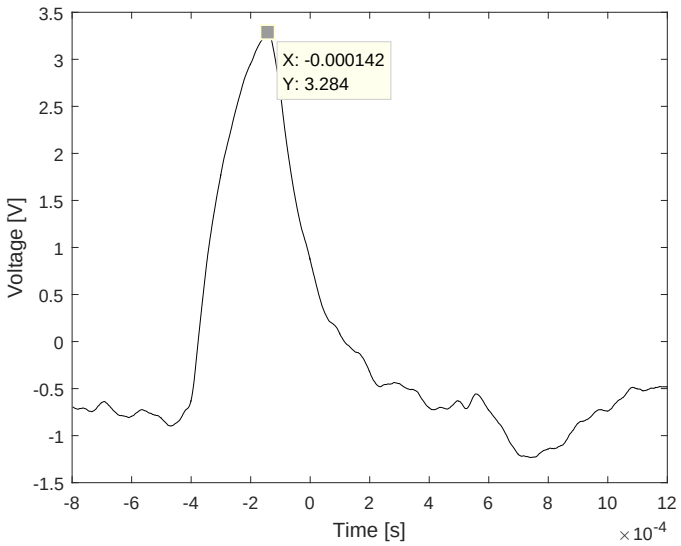

Figure 17. Example of a valid pulse. Pulses used to test the validity of the original analysis algorithm were selected based off visual inspection. Only clearly defined pulses as shown above were selected for the validation.

Data sets were created based on the selected valid pulses and the average pulse maximums were calculated. With known V_{max} values, the pulses were then analyzed using the original algorithm. Upon inspection, it was revealed that in both data sets, a significant number of pulses were excluded from the algorithm's analysis, which ultimately returned a value of '0' for V_{max}. The original algorithm excluded 17/99 pulses from the first data set and 19/94 from the second. Additionally, the average V_{max} returned from the code resulted in approximately 14% error when compared to the average V_{max} from the manual calculations. In order to capture these missed pulses, the code was modified to better model the exponential pulse decay and amplitude. The improved code captured all pulses and returned a more accurate V_{max}. The

V_{max} error was reduced to approximately 2.8–4.2% when compared to the manual calculations. These results are summarized in Table 6 and Figure 18

Table 6. The average V_{max} values were calculated from two data sets for raw data, the original algorithm, and the improved algorithm.

	Raw data	Original Algorithm	Improved Algorithm
Average V_{max}	3.04 / 3.11	2.61 / 2.71	3.17 / 3.2
Std dev	0.48 / 0.53	1.44 / 1.17	0.68 / 1.01
Average % difference from raw	–	14.1 / 12.8	4.3 / 2.8

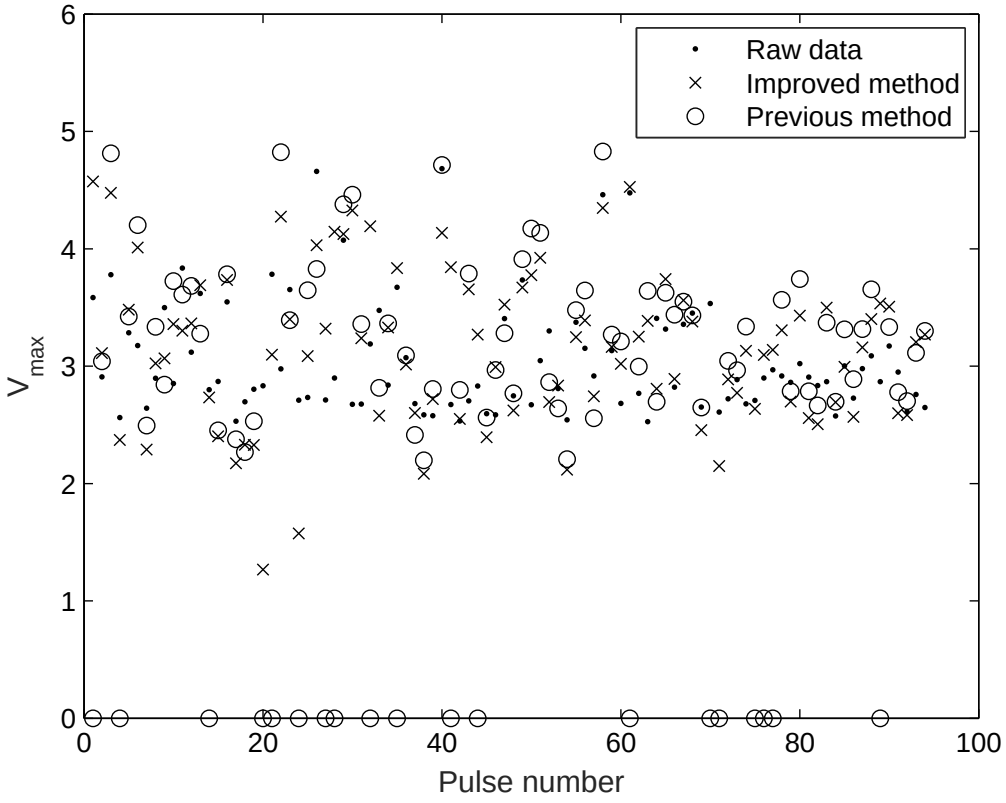

Figure 18. A comparison of original and improved algorithms for analyzing V_{max}. For this data set, the original algorithm excluded 19/94 pulses, indicated by the '0'-values along the x-axis. The improved algorithm captured all pulses.

Decay time was calculated for each data point along the fall time curve using (8) and then averaged. Because the original algorithm determined τ from the V_{max} data, any V_{max} value equal to zero also returned a τ value of zero.

$$\tau = -\frac{V_o}{\frac{dv}{dt}} \tag{8}$$

In order to increase accuracies in decay values, a more precise V_{max} was preferred. The algorithm was further improved to only accept valid pulses. Each data set contains pulses, which upon visual inspection could be categorized one of three ways. Pulse categories are summarized in Table 7.

Table 7. Summary of pulse categories and their description.

Pulse Type	Description
Valid	Pulses in this category had clear rise and fall times and were distinct from other features.
Clipped	Pulses in this category had clear rise and fall times, but had no discernible maximum.
Invalid	Pulses in this category are highly irregular and do not meet any of the other criteria.

Figure 19 illustrates an example of each type of pulse. An algorithm was developed which discriminated valid pulses from other pulses and returned the pulse V_{max}.

3.10 Environmental Testing

The crystal holder was placed in a glove bag in order to assess environmental effects on data collection. The glove bag was filled with dry nitrogen and data sets were collected under a controlled relative humidity of 48-52%. This relative humidity closely replicated normal laboratory conditions. The glove bag was then filled with silica gel packets in order to evacuate moisture inside the bag.

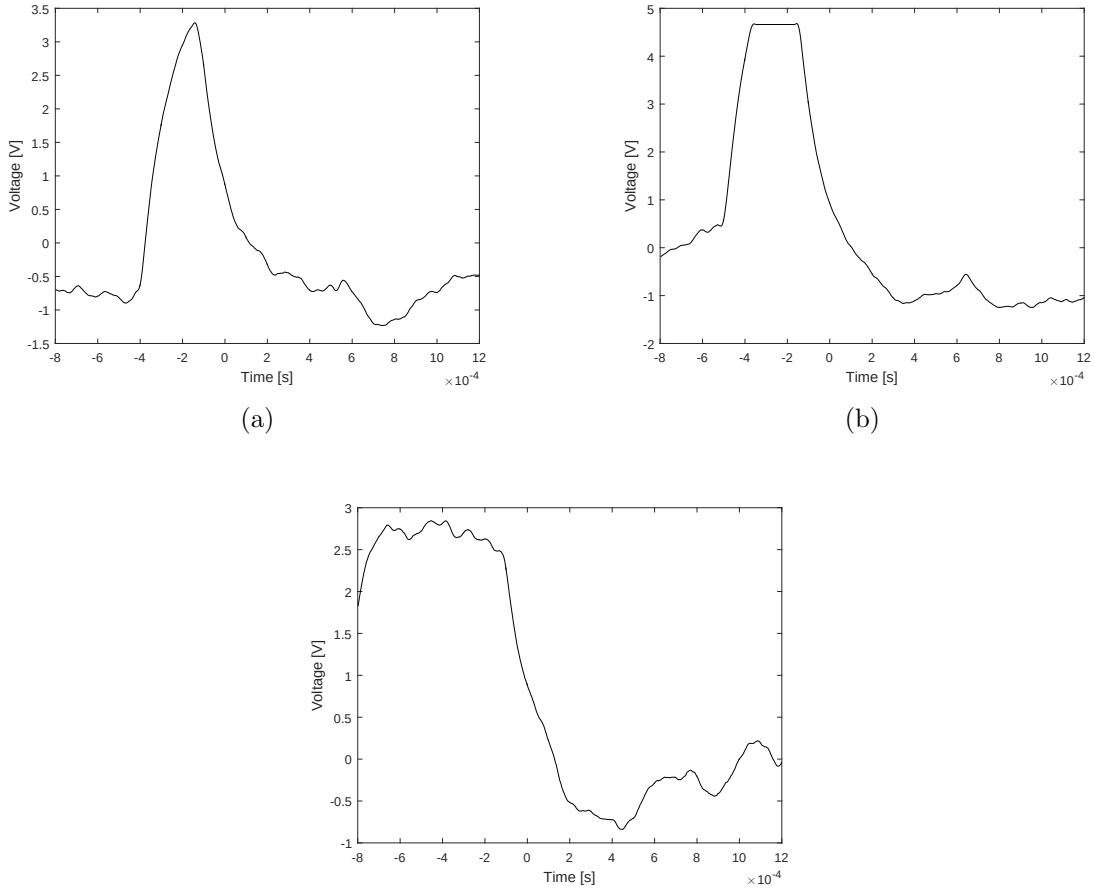

Figure 19. Plots of representative pulse examples: (a) valid pulse, (b) clipped pulse, and (c) invalid pulse.

The glove bag was then refilled with dry nitrogen and data sets were collected again under a relative humidity of 15–22%. This relative humidity is extremely low for laboratory conditions. Irradiation and data collection was conducted with the procedures previously described.

3.11 Statistical analysis of data

The Kilmogorov-Smirnov test (KS-test) and a variation of the KS-test were used to quantitatively determine whether the crystal responded differently to each radiation type. The KS-test can be used to determine whether or not a sample comes from a population with a specific distribution. Because the distribution of data was unknown and could theoretically change based on radiation type, the distribution of data could not be modeled. The KS-test does not require any particular data distribution. Rather, the univariate KS-test only relies on two assumptions.

1. The data ($X_1, X_2..., X_m$ and $Y_1, Y_2..., Y_n$) are independent random samples from continuous populations.

2. The X's and Y's are mutually independent from each other.

In general, the univariate KS-test compares the absolute difference between cumulative distributions against a null hypothesis that samples are drawn from the same distribution. This makes the KS-test a very robust test and ideal for this experiment. An overview of this concept is diagrammed in Figure 20.

Multivariate KS-test

Data sets were large, each set generally ranging between 28,000-32,000 pulses. Each pulse analysis produced two parameters: V_{max} and τ. While there are numerous tests which rely on univariate variables, there are very few methods which

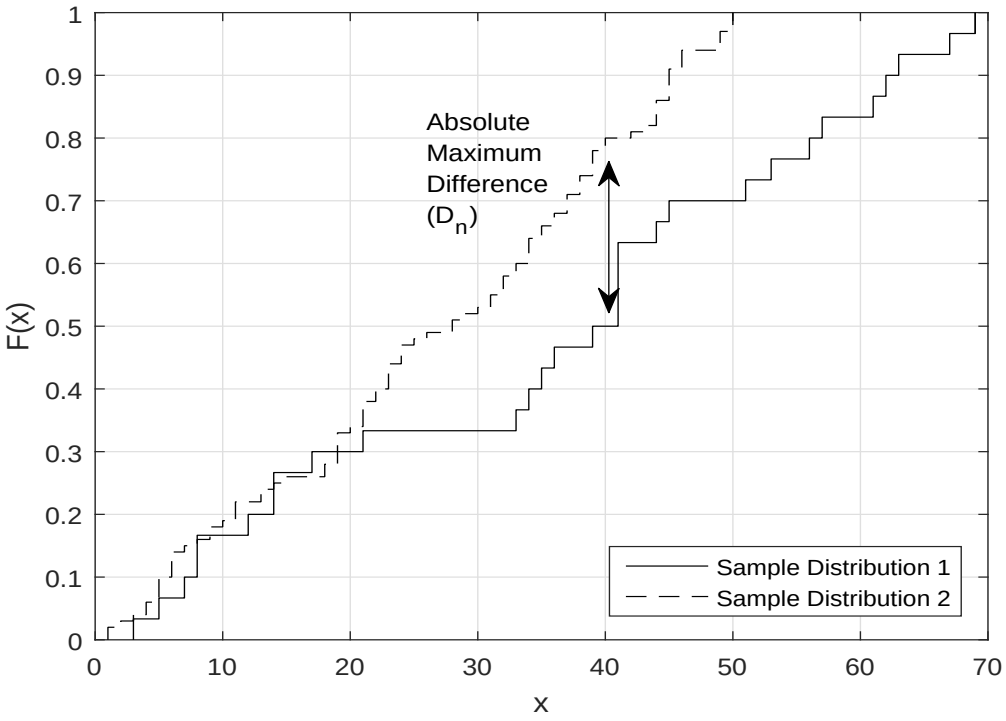

Figure 20. Graphical representation of the Kilmogorov-Smirnoff test in one dimension. The test compares the the cumulative distribution from each data set and returns a statistic based on the maximum difference (D_n) between the two distributions.

analyze multivariate variables. In order to analyze these data sets, a modified KS-test developed by Peacock was employed [28].

The multivariate KS-test is a modification of the univariate KS-test. The algorithm employed by Peacock is shown below.

1. Find D_n, the maximum absolute difference in the two cumulative probability distributions being compared, all four possible ranking combinations being considered.
2. Set $Z_n = \sqrt{nD_n}$ and convert Z_n to Z_∞ by $1 - Z_n/Z_\infty = 0.53n^{-0.9}$.
3. Calculate the significance from $P(> Z_\infty) = 2e^{-2(Z_\infty - 0.5)^2}$.
4. For a two sample test, replace n by $n_1 n_2/(n_1+n_2)$, provided n_1 and n_2 >10. [28]

Validation of the Multivariate KS-test

An algorithm using Peacock's method was written and developed by Muir [29]. With the null hypothesis being that the data is from the same distribution, the algorithm returned the KS-statistic as well as acceptance or rejection of the null hypothesis. Rejection of the null hypothesis means the data comes from different distributions. In order to test the validity of the script, several data sets were generated. Additionally, the multivariate KS-test was applied to the crystal data. These tests are discussed below.

Data Sets from a Random Number Generator

Two data sets, each consisting of a 1,000×2 matrix, were created by using MATLAB's "randi" function. 1,000 integers were randomly selected ranging between 1 and 100, forming one dimension, 1,000 integers were randomly selected ranging between 1,000 and 4,000, forming the second dimension. These data sets were generated and tested 100 times using the multivariate KS-test, with α set to 0.05. Only once did the test reject the null hypothesis, with a test statistic of 0.009.

Data Sets from the Same Distribution

It was expected that pulses generated during the same irradiation experiment come from the same distribution. In order to validate this, data generated from the same experiment were split evenly into two data sets. In order to ensure uniform sample distribution, odd numbered pulses generated the first data set, even numbered pulses generated the second set. This ensured that any pulse variance over time was sufficiently captured in each data set. Table 8 summarizes the results of the multivariate KS-test.

Table 8. KS-test results applied to same data set. The KS-test accepted the null hypothesis on each measurement with varying alphas indicating data came from the same distribution.

Data set	α	**Accept / Reject H_0**
Background	0.1 /0.05	Accept / Accept
Alpha Irradiation	0.1 /0.05	Accept / Accept
Gamma Irradiation	0.1 /0.05	Accept / Accept

4. Results

4.1 General

The UO_2 crystal was irradiated numerous times. Early experimental analysis revealed the electronic response (e.g. noise) was extremely sensitive to contact placement. For consistency, data comparisons were made only with data taken with the same probe contact locations. Each time the crystal/probe system was moved (such as during transport) an entire data set, including background, was collected. This substantially increased data collection requirements, but ensured that comparisons were made with like data responses.

Table 9 outlines each experiment and how many times each measurement was recorded. Experiments 1–6 were conducted under ambient temperature and humidity conditions. Experiments 7–8 were conducted inside of a glove bag which regulated humidity. Each experiment was designed to answer specific questions which are summarized below.

1. Experiment 1: Is the crystal responding to radiation? This experiment determined whether radiation produced a response within the crystal.

2. Experiment 2: Can fast neutrons be detected? The result of this experiment lead to the hypothesis that environmental factors could have a significant impact on crystal response and pulse collection.

3. Experiment 3–5: Probe contact location considerations. This experiment determined that probe contact locations directly affect pulse collection.

4. Experiment 6: Is the crystal still responding after neutron irradiation? Several collection variables had changed and this experiment was conducted in order re-establish a baseline response.

5. Experiment 7(1): Does aridity affect signal collection? This experiment was conducted in a glove bag under arid ($\sim$ 15–22% relative humidity) conditions.

6. Experiment 7(2): Does humidity affect signal collection? This experiment was conducted in a glove bag under ambient ($\sim$ 48–52% relative humidity) conditions.

7. Experiment 8(1–2): Can data from experiments 7(1) and 7(2) be reproduced? These experiments attempted to recreate data from experiment 7.

Table 9. Summary of experiments and types of measurements recorded.

Experiment	**Measurement**					
	Background	^{241}Am	^{241}Am w/shielding	^{55}Fe	^{60}Co	Neutron
1	2x	1x	2x	1x	1x	
2	5x	2x			1x	5x
3	1x					
4	1x					
5	1x					
6	2x	2x	1		2x	
7(1)	2x	2x			2x	
7(2)	2x	2x				
8(1)	2x	2x		2x	2x	
8(2)	2x	2x		2x	2x	

The results of the experiments lead to the following conclusions:

1. The noise and resulting waveforms are very sensitive to probe contact placement.

2. The radiation response from different types of radiation is unique within a data set.

3. The crystal response is sensitive to humidity. The environmental effect on the noise is most remarkable.

4. The result of detection experiments using fast neutrons were inconclusive.

These conclusions will be discussed below.

4.2 Crystal Probe System Considerations

The crystal was placed in the probe station and held in place with 0.635 mm tungsten probe tips. Once the crystal was placed, data collection could begin. Each data set was analyzed, which provided a count rate based upon the number of pulses counted during the counting time. Radiation detection was based on three assumptions:

1. Each source decays at a constant rate.

2. Each photon (or particle) has the same probability of being detected.

3. Charge collection occurred at a constant rate.

A count rate was calculated based on the number of pulses collected during the experiment. Each pulse was plotted based on the time it was collected. With the assumptions listed above, a generally smooth plot was expected from an irradiation experiment (Figure 21a). However, this was not the case for all experiments. Unexplainable gaps or irregularities in the counting plots can be observed during the experiments. Examples of these irregularities are plotted in Figure 21 (b-d).

From Figure 21, some experiments had numerous counting gaps during the counting time, some cyclic and others random. Large counting gaps are found in
Figures 21b and 21c and result in low count rates. This was indicative of poor probe contact with the crystal. Because of this, once the crystal was placed in the probe station, all efforts were made to ensure the crystal was not moved in any way during any experimental set.

While voltage fluctuations could contribute to small counting gaps, gaps in background measurements could also be a result of the low specific activity of the crystal. Additionally, the primary decay mechanism of ^{238}U is alpha decay. The specific activity of ^{238}U is 12,210 Bq g^{-1}. This specific activity results in an estimated crystal

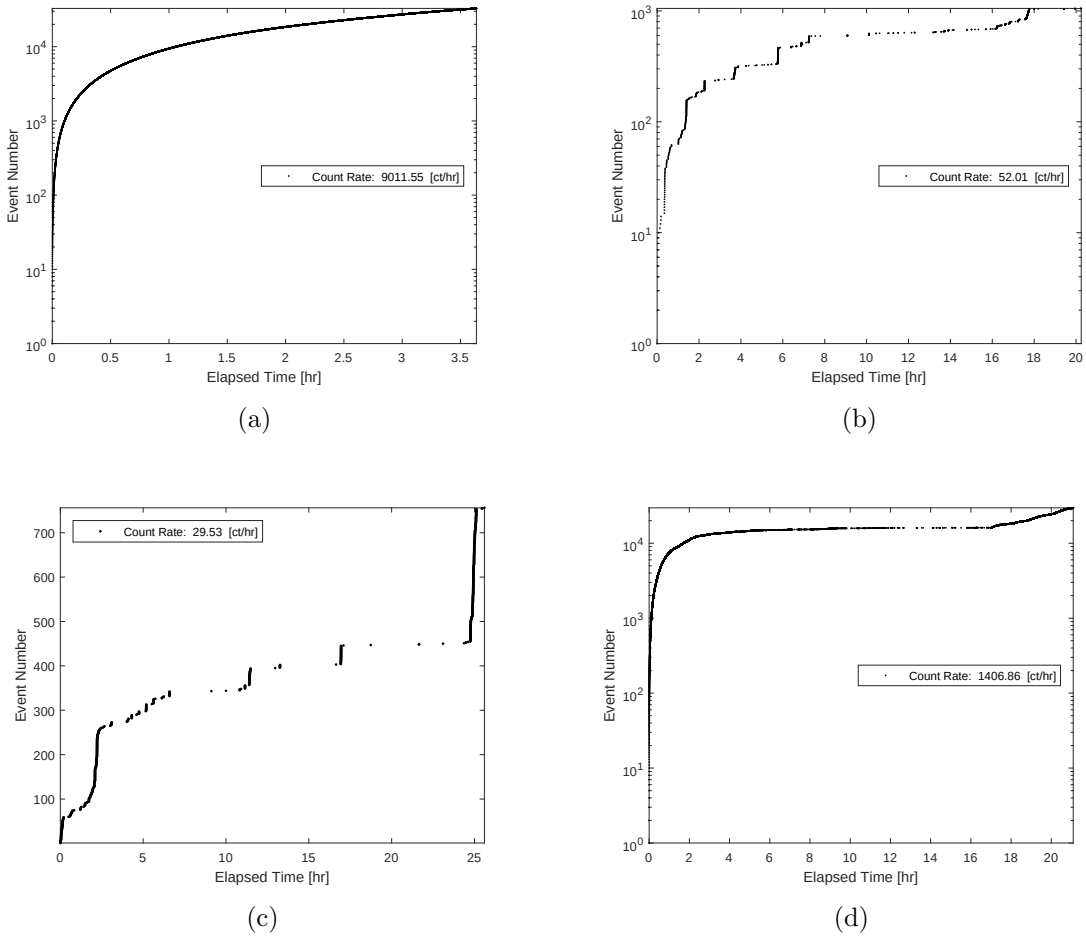

Figure 21. Figure (a) is an example of an expected irradiation measurement. Both exposure and charge collection remain approximately constant. Figures (b) and (c) plot examples of low count rates. Numerous gaps and stair-step spikes are indicative of poor probe contract. Figure (d) highlights random gaps, indicative of voltage fluctuations.

activity of 132 Bq. This activity is relatively low when compared to some alpha emitters. It is possible that conduction electrons generated from alpha particle interactions along the crystal periphery are not collected by the probe tips, indicating a low active detective region within the crystal.

According to SRIM calculations, 4 MeV alpha particles have an approximate range of 8.67 μm. The energy transferred from the alpha particle excites valence electrons into the conduction band. Once in the conduction band, and under an applied electric field, the electrons travel a distance until they recombine. This distance is substantially influenced by the carrier mobility and lifetime. If the distance traveled is not within the active detection volume of the crystal, the charge will not be collected. Additionally, the tungsten probe tips in contact with the crystal were $\sim$ 0.635 mm in diameter and only made contact with a very small area of the crystal surface. Thus, the electric field held at a potential of 4.5 V, may not sufficiently influence the charge carriers. This concept is illustrated in Figure 22.

Some experiments produced counting plots with random counting gaps and sudden periods of high count rates during data collection. An example of such a period is plotted in Figure 23. The high count rate in Figure 23 occurs around the fifth measurement hour.

The cause of the random counting gaps and sudden count rate increases is undetermined. These could be attributed to fluctuations in the high voltage power supply. Although the power was connected to a power conditioner set to output 115 V, fluctuations of up to 3 V were observed in the power conditioner readout. These fluctuations were random and could not be controlled. It is expected that these fluctuations were eventually transferred to the bias on the UO_2 crystal which ultimately affected charge collection (gaps) and rate of charge collection. Because of this, experiments 3-8 were not connected to the power conditioner.

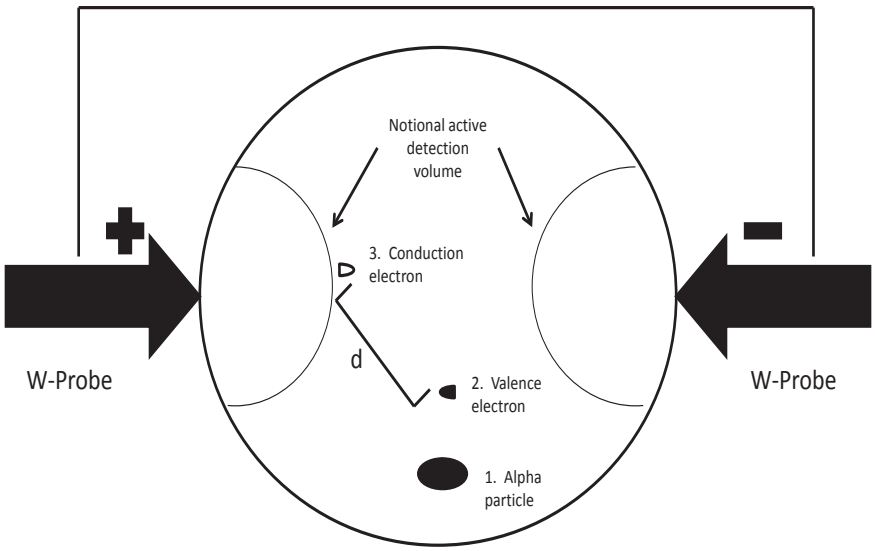

Figure 22. Diagram showing notional crystal active detection volume. The energy from an alpha particle Coulombic interaction (1) excites valence electrons (2) into the conduction band. Once in the conduction band, a conduction electron (3) will travel a certain distance, 'd', before recombining. If this distance is not within the active detection volume, the charge will not be collected.

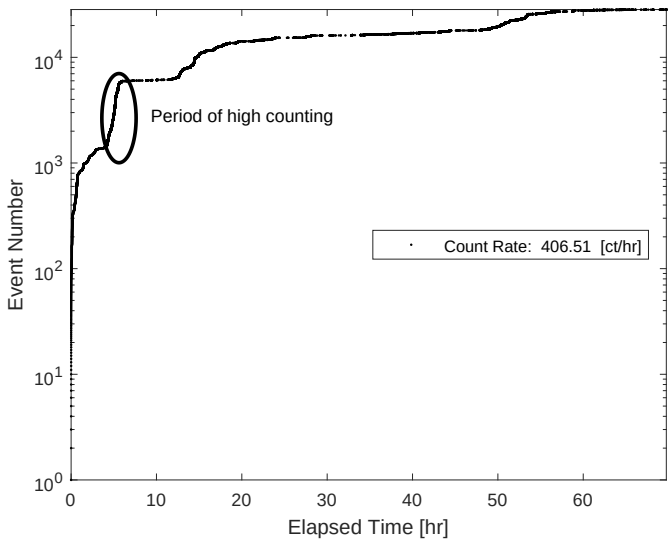

Figure 23. Example of a period with a high count rate. The sudden increase in measured pulses occurs around the fifth hour. These sudden increases are believed to be caused by a combination of poor probe contact and voltage fluctuations.

It is impossible to place the contact probes exactly in the same location after the crystal was removed. In order to ensure data could be compared, new data sets composed of background, alpha, and gamma irradiations were collected each time the contact location changed.

4.3 Crystal Response to Different Forms of Ionizing Radiation

A hypothesis of this research was the crystal will respond to neutrons. Each type of radiation interacts differently with material and therefore can generate charge carriers differently within the medium. Because of this, the crystal was exposed to alpha, gamma, and neutron radiation.

Correlation between counting rates

The counting plots provided information as to how the crystal responds to radiation. The activity of each source provided an expectation of intrinsic detector

efficiency. Table 10 summarizes the activity of each source, the expected number of pulses, and the average number of pulses recorded from each experiment. The expected number of pulses assumes 100% geometric and intrinsic efficiencies. The geometric efficiency assumes all radiation quanta based on the solid angle from the source strike the detector. The intrinsic efficiency assumes all radiation quanta produce a pulse within the detector. None of the experiments resembled the expected count rates in Table 10.

Table 10. Summary of source activity. The starred (*) ^{60}Co was used in warehouse experiments and had a different activity than that used in the laboratory.

Type of Exposure	Activity [Bq]	Distance from detector [mm]	Solid Angle [sr]	Expected Counts [ct/hr]
^{241}Am	36,783	1	6.63×10^{-1}	6.9899×10^{6}
^{55}Fe	1.62×10^{6}	25.4	1.217×10^{-3}	5.658×10^{6}
^{60}Co	1.306×10^{5}	25.4	1.217×10^{-3}	4.553×10^{5}
^{60}Co*	9.879×10^{4}	25.4	1.217×10^{-3}	3.444×10^{4}
^{252}Cf	6.656×10^{7}	25.4	1.217×10^{-3}	2.321×10^{7}

Correlation between V_{max} and τ using original algorithm

From Young's work [24], it was believed there was a general correlation between the pulse V_{max} and τ. The general trend in Young's research was that pulses with higher V_{max} correlated to smaller τ. This was generally true for all radiation. Figure 24 gives examples of results for ^{55}Fe and ^{241}Am irradiation experiments analyzed using Young's algorithm. The V_{max}/τ correlation, however, was reversed for the ^{60}Co experiments. Figure 25 compares the results of two different ^{60}Co measurements from experiments 1 and 6.

It is unclear as to why the V_{max}/τ correlations are reversed in Figure 25, but the phenomenon was consistent with various crystal configurations. The reversed

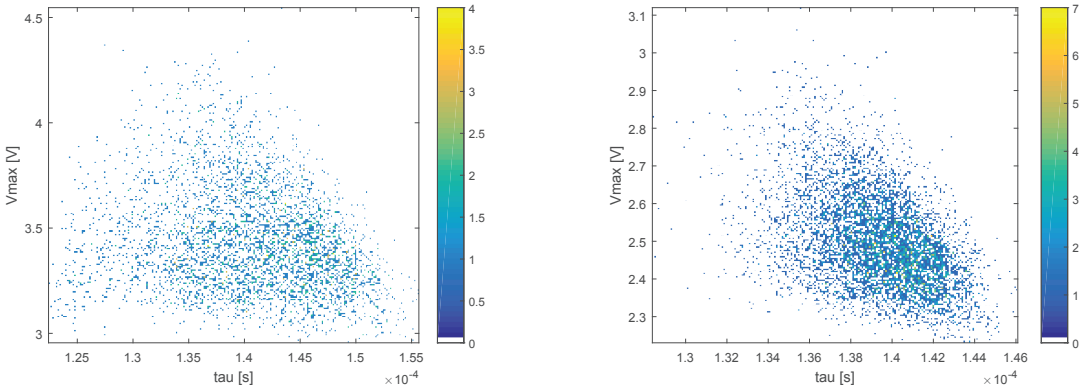

(a) (b)

Figure 24. V_{max} and τ histograms for a) ^{55}Fe and b) ^{241}Am: histograms were produced using the original algorithm. There is a general correlation between higher V_{max} and shorter τ.

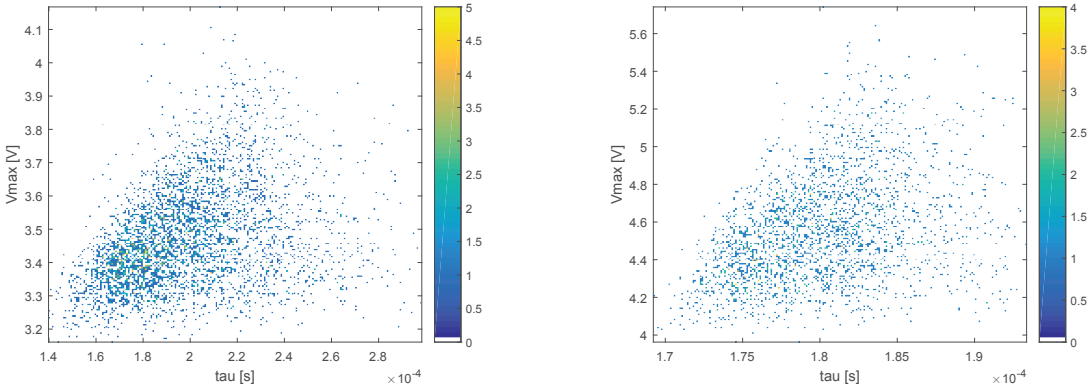

(a) (b)

Figure 25. V_{max}/τ histograms for ^{60}Co: histograms were produced using the original algorithm. Plots were generated using data from two different experiments. For high energy photons, there is a general correlation between higher V_{max} and longer τ.

V_{max}/τ correlations could be attributed to the high gamma energy from the ^{60}Co source. Compared to ^{55}Fe, the gammas from ^{60}Co are approximately 238 times more energetic. The low energy gammas from ^{55}Fe, as well as the high energy alpha particles from ^{241}Am, are not as penetrating in UO_2. The low penetrating power would result in a large amount of energy being deposited over a short distance. In the case of ^{60}Co, the radiation would penetrate much further into the UO_2 crystal, which could result in increased electron scattering and broadened pulse decays.

Analysis of Improved Algorithm

The original algorithm was modified to analyze valid pulses only. Therefore all data were reanalyzed for evidence which correlated V_{max} and τ. Figure 26 presents a ^{60}Co and ^{241}Am measurement analyzed using the original and improved algorithm. The histograms produced using the original algorithm are on the left (a and c); those histograms produced using the improved algorithm are on the right (b and d) and are substantially different.

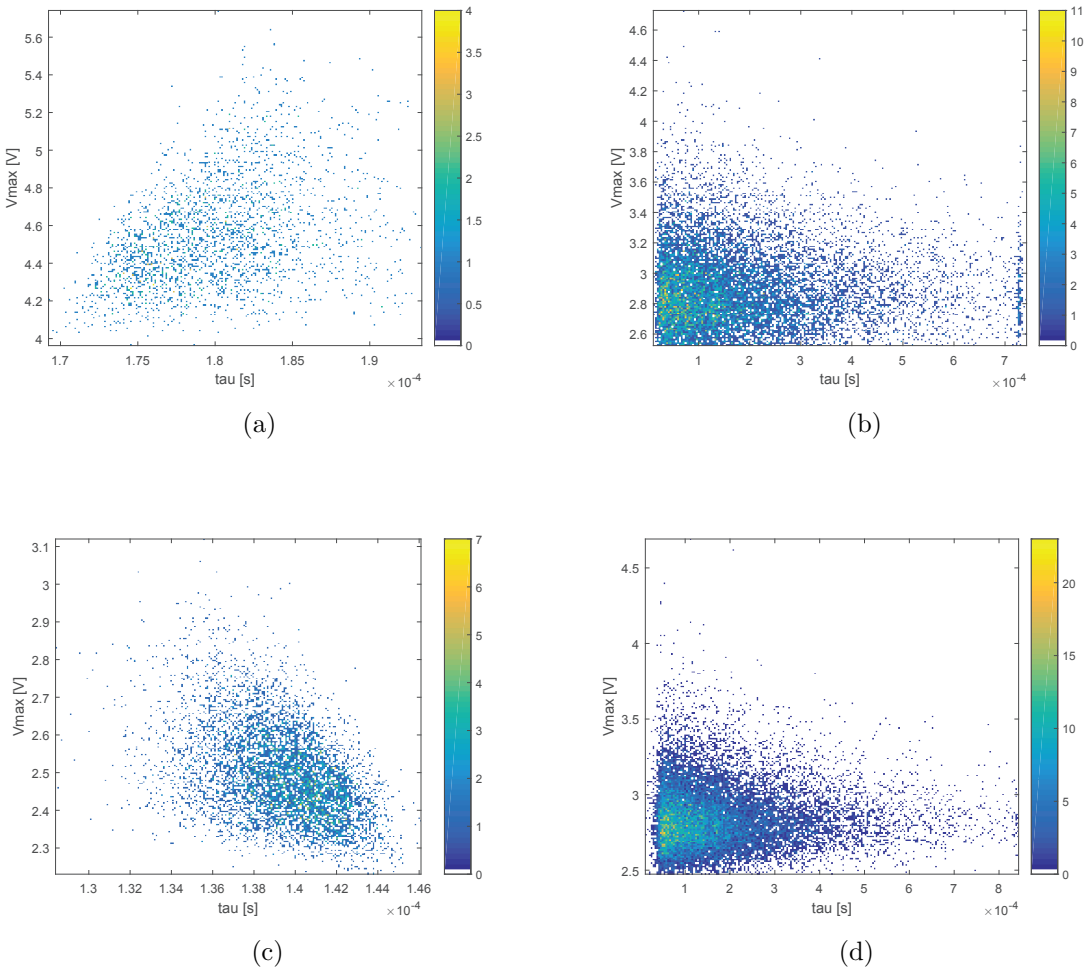

Figure 26. Comparison of V_{max}/τ histograms obtained using the improved analysis algorithm. Histograms using the original algorithm are on the left; histograms on the right are from the improved algorithm. (a-b) Histograms resulting from a ^{60}Co measurement. (c-d) Histograms resulting from an ^{241}Am measurement. From visual inspection, the two algorithms produce vastly different histograms.

It is apparent the two algorithms are producing different results. The cause for the large difference in histograms was primarily due to an error in the original algorithm in which incorrect data (clipped and invalid pulses) was analyzed. Once the error was corrected, the entire histogram changed shape. The axes changed as well, resulting in a much broader range of V_{max} and τ values.

Correlation between V_{max} and τ using improved algorithm

All data sets were re-analyzed using the improved algorithm. Figure 27 represents V_{max}/τ histograms from background, ^{60}Co, and ^{241}Am measurements. Unlike the original algorithm, there is no clear correlation, based on visual inspection, between a pulse V_{max} and its τ.

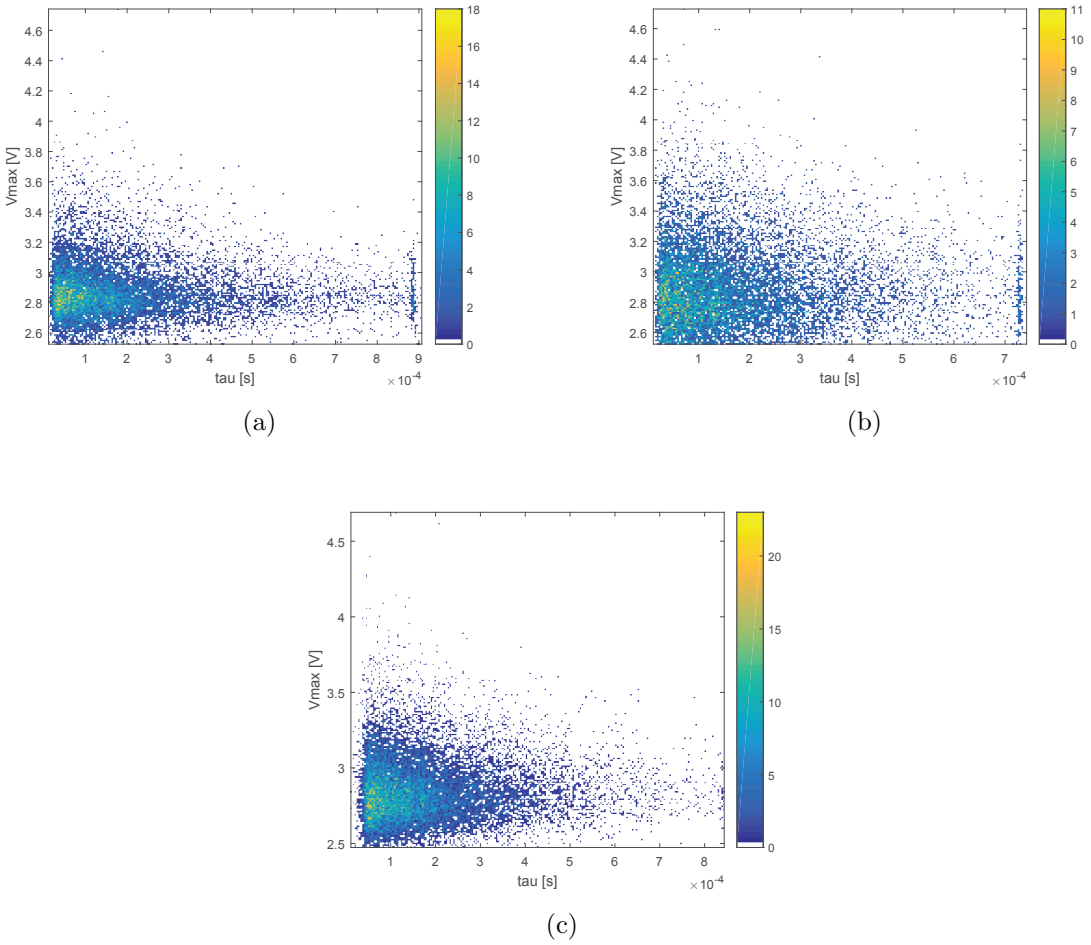

Figure 27. Example V_{max}/τ histograms produced using improved pulse analysis algorithm. (a) Results from a background measurement. (b) Results from a ^{60}Co measurement. (c) Results from an ^{241}Am measurement. Histograms do not have a defined shape as in previous histograms produced from the original algorithm.

In all histograms, however, a reoccurring phenomenon appears on the far right (highest values in τ) of each plot and forms a vertical clustering of data. This phenomenon is illustrated in Figure 28. The intensity of this phenomenon varies between

measurements. The location, however, is always at the upper τ boundary, which varies by measurement. The cause of this phenomenon is unknown, but may be indicative of pulse tailing.

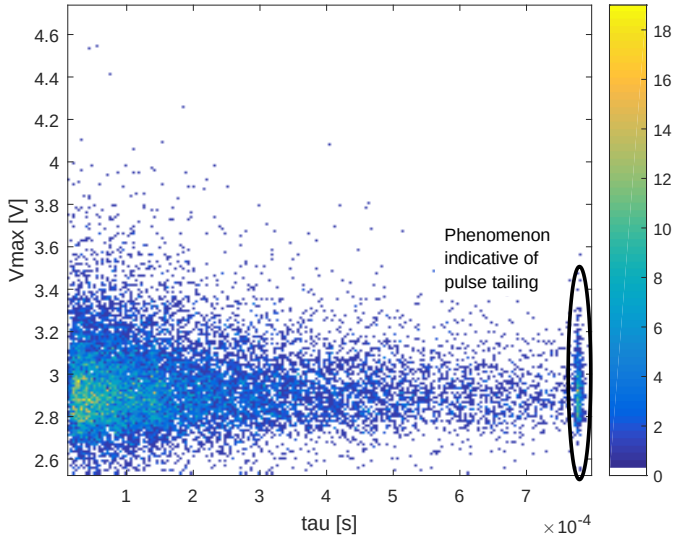

Figure 28. Phenomenon seen in all histograms. The phenomenon occurs at the extreme upper τ values and varies in intensity. This phenomenon may be an indicator of pulse tailing.

Multivariate KS-test Results

V_{max}/τ histograms are qualitative. The multivariate KS-test was employed in order to quantitatively assess whether data sets are statistically different. Data from experiments 1 and 6 were compared. These experiments were analyzed because they were acquired in the same laboratory (discussed later). The results from each experiment are summarized in Table 11.

The results in Table 11 only compare data generated from the same experiment. Data can only be compared across the contact probe location for the results to be meaningful, as the crystal is sensitive to contact placement. The results from Table 11 strongly suggest the crystal responds differently to different forms of ionizing radiation. This is further substantiated by the multiple ^{60}Co experiments. Data

Table 11. Summary of multivariate KS-test results. The test reveals that V_{max}/τ distributions between sources may be unique. In one comparison of ^{60}Co experiments, the test accepts the null hypothesis, indicating the distributions are the same.

Experiment	Comparison	P-value	Accept / Reject H_0
1	Background – ^{241}Am	$<1\times10^{-3}$	Reject
	Background – ^{60}Co	$<1\times10^{-3}$	Reject
	Background – ^{55}Fe	$<1\times10^{-3}$	Reject
	^{241}Am – ^{60}Co	$<1\times10^{-3}$	Reject
	^{241}Am – ^{55}Fe	$<1\times10^{-3}$	Reject
	^{60}Co – ^{55}Fe	$<1\times10^{-3}$	Reject
6	Background – ^{241}Am	$<1\times10^{-3}$	Reject
	Background – ^{60}Co	$<1\times10^{-3}$	Reject
	^{241}Am – ^{60}Co	$<1\times10^{-3}$	Reject
	^{60}Co (1) – ^{60}Co (2)	$<1\times10^{-3}$	Reject
	^{60}Co (1) – ^{60}Co (3)	**0.0869**	**Accept**
	^{60}Co (2) – ^{60}Co (3)	$<1\times10^{-3}$	Reject

generated from the same radiation source should have the same V_{max}/τ distribution; one comparison between two ^{60}Co measurements was accepted, indicating data came from the same distribution.

While the results from the multivariate KS-test suggest that bivariate histograms can be used to distinguish radiation types, there are several limitations to the multivariate KS-test. The multivariate KS-test algorithm is limited to a p-statistic of 0.2. When this limitation is removed, the test can return nonsensical results, as the p-statistic cannot exceed "1". Additionally, Peacock's algorithm was developed for comparisons where sample sizes are extremely small, yet the sample sizes tested are orders of magnitude larger (N>10,000). This method is relatively untested and may either not be applicable to large sample sizes or, more likely, too sensitive. Because of this, alternative methods were also employed to analyze data.

Analysis of Pulse Amplitude and Pulse Decay Time

Rather than discerning discrete differences in a multivariate histogram, the individual components (V_{max} and τ) were examined independently of one another. Under current experimental procedures, V_{max} may not discriminate radiation types as well as τ. These results are discussed below.

Analysis of V_{max}

All data were generated using specific trigger settings. These settings were chosen based on early experimentation with the crystal. In order for the oscilloscope to record an event, a pulse had to cross two amplitude thresholds: 0.88 V and 2.39 V. These trigger settings explain why each of the plots in Figure 27 contain a large cluster of events in the 2–3 V range. This is further illustrated in Table 12.

Table 12. Summary of V_{max} values. With the exception of one ^{241}Am experiment, the average V_{max} ($\overline{V_{max}}$) values are all within 3% of each other and almost 2/3 of all pulses lie between the trigger setting and the average V_{max}.

Measurement	$\overline{V_{max}}$ [V]	Fraction of Pulses 2.39–$\overline{V_{max}}$	Fraction of Pulses > $\overline{V_{max}}$
^{241}Am	3.35	0.58	0.42
	3.01	0.65	0.35
Background	3.00	0.65	0.35
	3.08	0.65	0.35
^{60}Co	3.02	0.65	0.35
	3.05	0.62	0.38
	3.01	0.65	0.35
Average	3.07	0.64	0.36

Table 12 provides information regarding V_{max} values across all experiments. The average V_{max} ($\overline{V_{max}}$) values are approximately the same. This is further illustrated in Figure 29 which compares the normalized probability distributions of pulse V_{max}

between sources. Figure 29a shows ^{241}Am compared with background, Figure 29b shows ^{241}Am compared with ^{60}Co, and Figure 29c shows background compared with ^{60}Co data. All data presented are from experiment 6. These plots generally agree with each other. The cumulative distributions of V_{max} from all three sources are compared in Figure 30 and are practically identical.

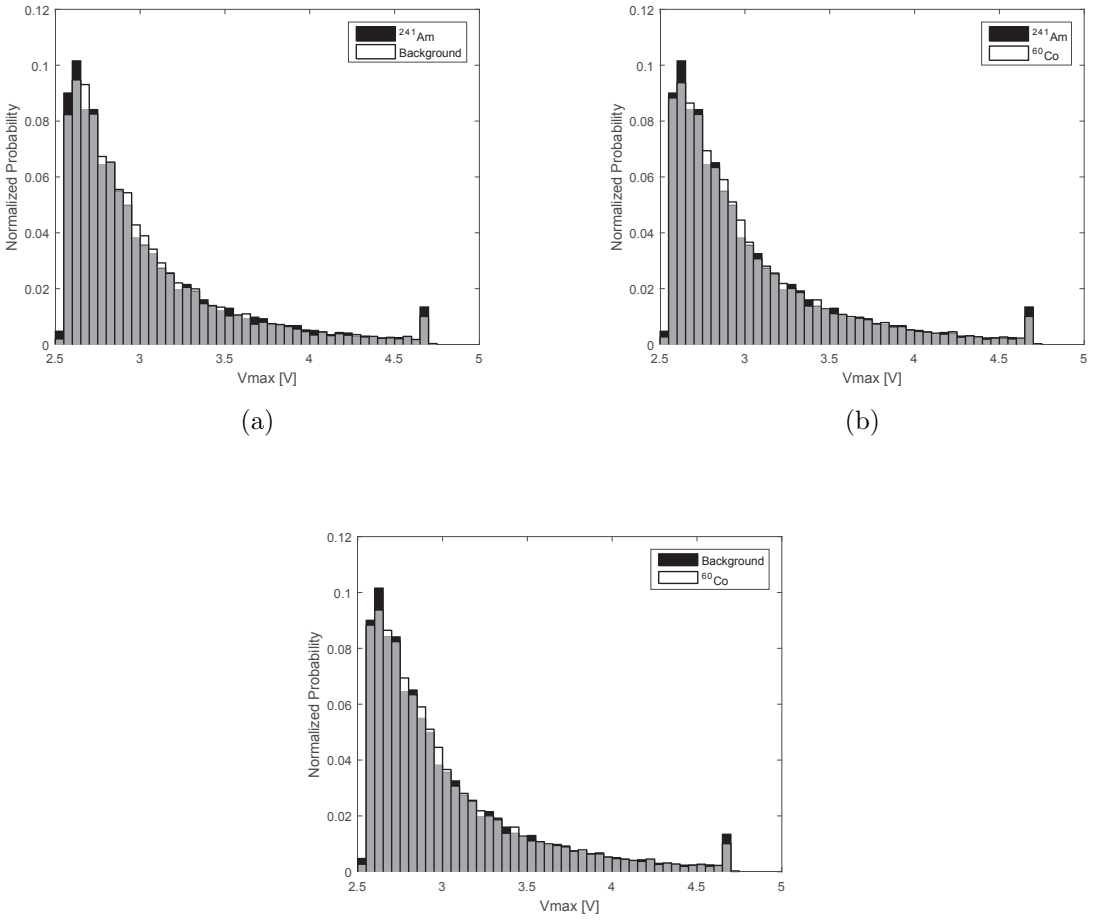

Figure 29. Comparison of V_{max} probability distributions between experiments. Figure (a) compares ^{241}Am to background, (b) compares ^{241}Am to ^{60}Co, and (c) compares background to ^{60}Co data.

The univariate KS-test statistically confirmed the similarities observed in Figure 30. The KS-test alpha parameter was set to 0.01 for every experiment. Table 13 summarizes the results from each test.

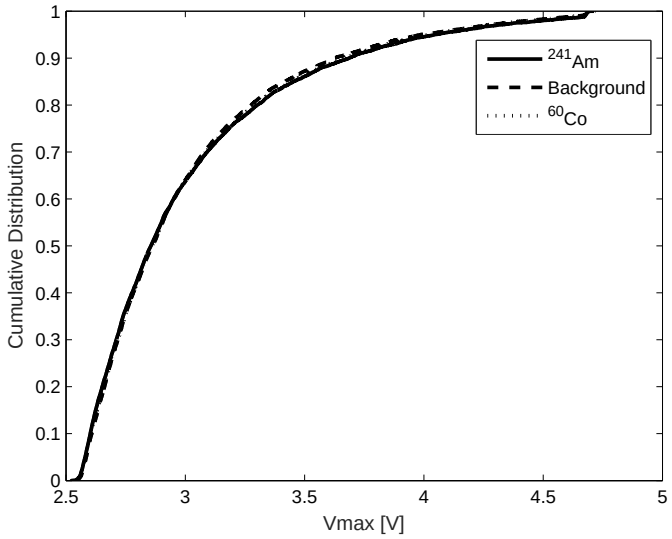

Figure 30. Cumulative distributions of V_{max} values from a background, ^{241}Am, and ^{60}Co measurement. The cumulative distributions of all three measurements are very similar. The KS-test accepts the null hypothesis for every comparison between the sources. These results suggest that separating radiation types using V_{max} is not practical.

Table 13. KS-test summary for V_{max} comparisons. Alpha was set to 0.01. In every case, the KS-test accepts the null hypothesis. This implies that V_{max} comparisons are not practical with current settings.

Comparison	Accept / Reject H_0	P-value
^{241}Am-^{60}Co	Accept	0.11
^{241}Am-Background	Accept	0.013
^{60}Co-Background	Accept	0.55

The KS-test accepted the null hypothesis for each comparison. These results indicate pulse V_{max} between the sources are too similar. The current experimental procedures do not provide sufficient evidence that radiation can be distinguished using V_{max}, as there is no unique relationship.

Analysis of τ

The τ were analyzed for each measurement from experiment 6. The results are summarized in Table 14, which presents the average τ ($\overline{\tau}$), the fraction of pulses that are equal to or less than $\overline{\tau}$, and the fraction of pulses greater than $\overline{\tau}$.

Table 14. Summary of τ values from experiment 6. Unlike V_{max}, τ values may be different enough to separate which could be useful in distinguishing radiation types.

Measurement	$\overline{\tau}$ $[1 \times 10^{-4} s]$	Fraction of Pulses $\leq \overline{\tau}$	Fraction of Pulses $>\overline{\tau}$
^{241}Am	1.2	0.59	0.41
	1.59	0.57	0.43
Background	1.56	0.58	0.42
	1.58	0.56	0.44
^{60}Co	1.52	0.57	0.43
	1.41	0.57	0.43
	1.52	0.56	0.44

Approximately 55% of pulses had decay times equal to or less than $\overline{\tau}$ (unlike V_{max}, where $\sim 65\%$ of data were within a minimum and average value). This data suggests there is greater variation within τ and may make it possible to distinguish radiation forms. A closer inspection of pulse decay distributions highlights these differences.

Like-Source Comparisons

Radiation and background τ distributions were compared using like-source measurements. Figure 31 compares like-source measurements from experiment 6. Based on visual inspection, the background measurements (Figure 31a) and the ^{60}Co mea-

surements (Figure 31d) are very similar and generally agree with each other. However, the distributions of the ^{241}Am measurements (Figure 31b) and one ^{60}Co measurement (Figure 31c) do not agree. Upon further inspection, it was revealed that ^{241}Am measurement 1 and ^{60}Co measurement 2 had count rates exceeding 9,000 counts/hour. These data sets were collected in ambient laboratory conditions and the excessive count rate is an indicator of an environmental change (discussed later) in the laboratory, resulting in differences in the τ distributions.

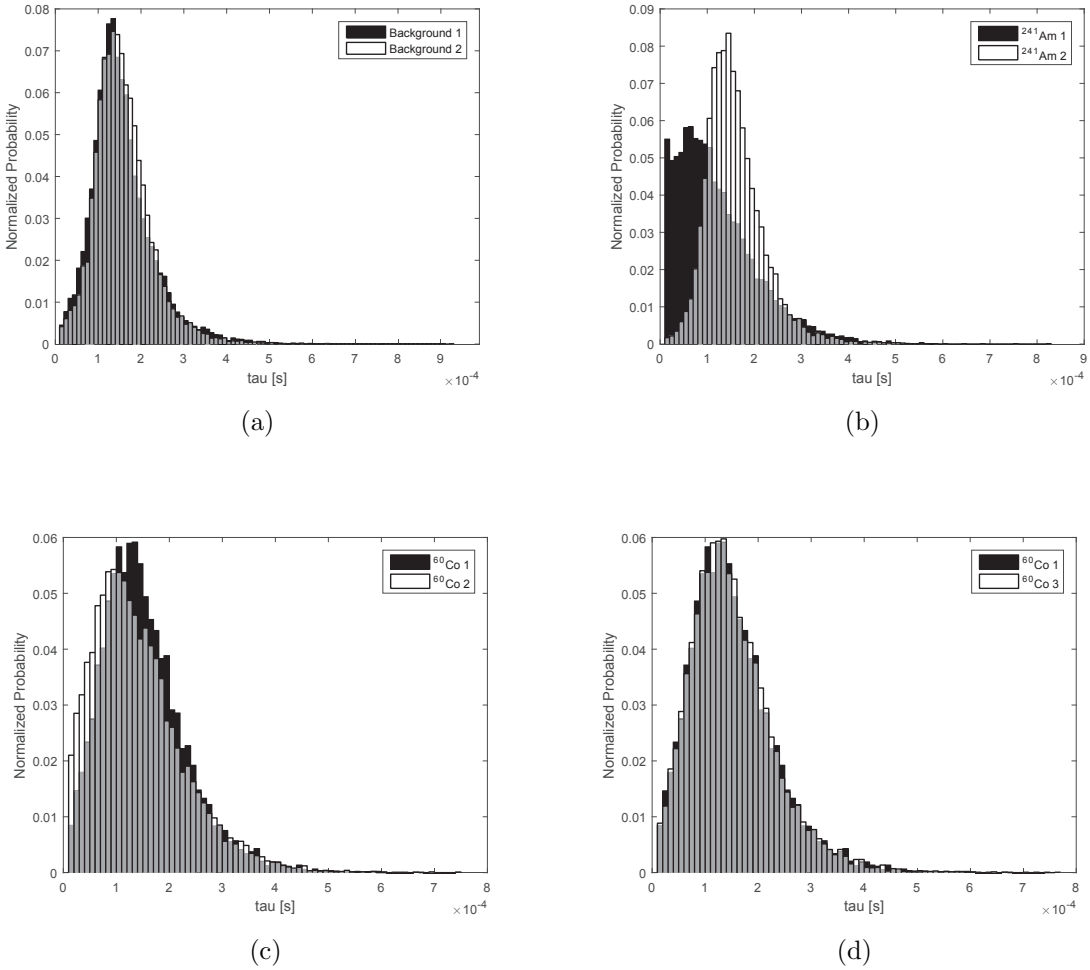

Figure 31. Comparison of τ probability distributions between like-measurements. Figures (a) (background measurements) and (d) (^{60}Co measurements) generally agree with each other. Figures (b) (^{241}Am measurements) and (c) (^{60}Co measurements) have noticeable differences. These differences are attributed to environmental effects.

Figures 32a and 32b present the cumulative distribution plots for the background and ^{60}Co measurements, respectively. The similarity between each plot is an indication data are from the same source. When the KS-test is applied the ^{60}Co distribution, the null hypothesis is accepted. However, while the background distributions are visually similar, the KS-test rejects the null hypothesis.

The difference in background samples is expected. Background signals are largely random in nature. The differences between the two samples can be attributed to random fluctuations. Figure 32a also highlights the sensitivity of the KS-test when applied to large samples. Q-Q plots were used in order to examine subtle differences in the CDF (as in Figure 32a).

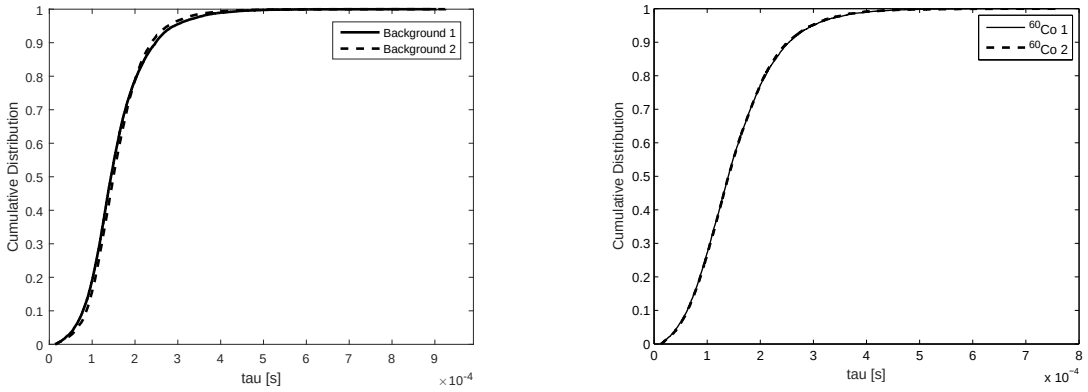

(a) (b)

Figure 32. τ cumulative distribution plots of (a) background and (b) ^{60}Co measurements. These CDF are suggestive that τ distributions may be unique for each type of measurement. This phenomenon suggests that radiation types can be distinguished based on their pulse decay times.

Q-Q plots are graphical representations of comparisons between two distributions. These plots are point-by-point comparisons between two probability distributions. Similar distributions result in a plot with a linear slope, although not necessarily along the line $y = x$. Figure 33 presents two separate Q-Q plots using example data.

Figure 33a compares two data sets from a similar distribution. The plot is linear, indicating the distributions are similar (in this example, the data are identical).

Figure 33b compares two data sets from different distributions. The plot has variations, particularly in the extreme lower and upper quantiles. In Figure 33b, data points above the line indicate probability is accumulating faster in sample distribution 4 (the y-axis); conversely, data points below the line indicate probability is accumulating faster in the sample distribution 3 (the x-axis). In each plot, the solid red line represents the 25-75th quantiles. Additionally, each plot has an R^2 value.

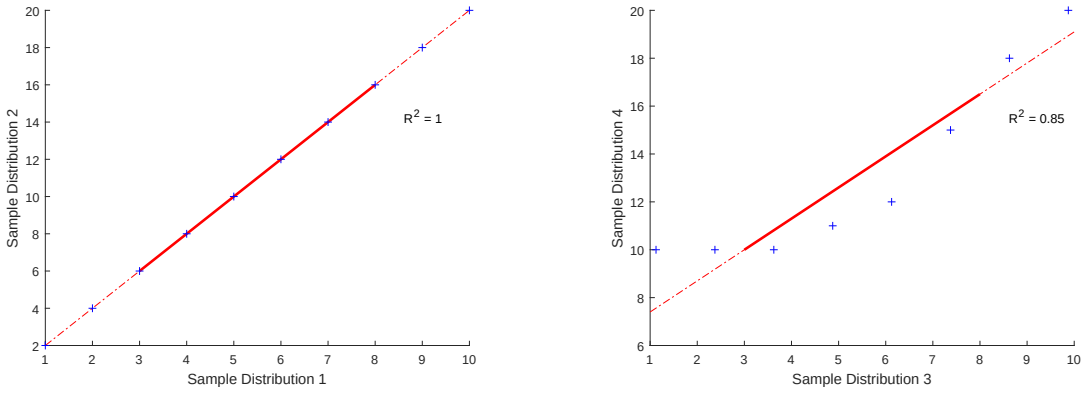

(a) (b)

Figure 33. Sample Q-Q plots: similar distributions are compared in (a). Different distributions are compared in (b).

Comparing the Q-Q plots may be beneficial when attempting to discern minor differences in cumulative distribution plots. The KS-test becomes more sensitive as sample sizes increase, causing the test to reject more null hypotheses. This is important because the UO_2 crystal is novel. As sample sizes increase, the KS-test rejects too many true null hypotheses which increases Type I error.

In order to reduce Type I error, the resulting R^2 value from Q-Q plots can be examined. In Figure 33a, the R^2 value is 1; in Figure 33b, R^2 value is 0.85. False rejections could be limited in future experiments by establishing an R^2 threshold. Using the example data in Figure 33b, a threshold of 0.99 would support rejecting the null hypothesis that data are from the same distribution.

Q-Q plots were used to analyze both the background data and the ^{60}Co data presented in Figure 31. The results are plotted in Figure 34. The R^2 value for background data (Figure 34a) is 0.997. The R^2 value for ^{60}Co data (Figure 34b) is ~ 1. Visually, there are outliers in the upper quantiles. These outliers do not affect the linear regression because there are few of them, compared to those on the line. By examining the R^2 value and overall shape, decisions can be made whether to accept or reject the KS-test statistics.

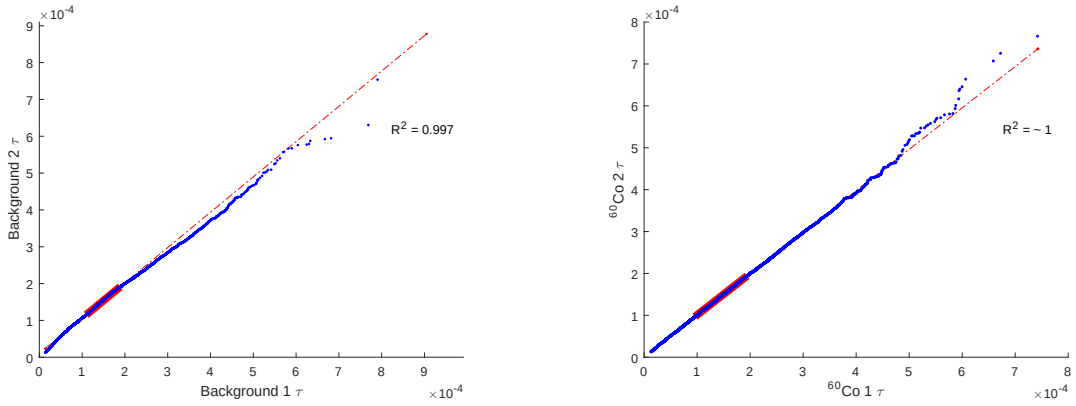

Figure 34. Q-Q plots from data: background distributions are plotted in (a). The R^2 value is 0.997. ^{60}Co distributions are plotted in (b).The R^2 value is $\sim$1.

Q-Q plot comparisons can be useful when comparing similar data. However, careful judgment needs to be exercised when establishing R^2 thresholds to accept or reject the KS-test statistic. The large number of samples can lead to high R^2 values even though the samples are different. This is demonstrated in Figure 35, which compares ^{60}Co to ^{241}Am distributions. The KS-test rejects the null hypothesis, the decay probabilities are clearly different (Figure 35a), but the R^2 value from the Q-Q plot (Figure 35b) is nearly linear. The key differences lie in the lower and upper quantiles.

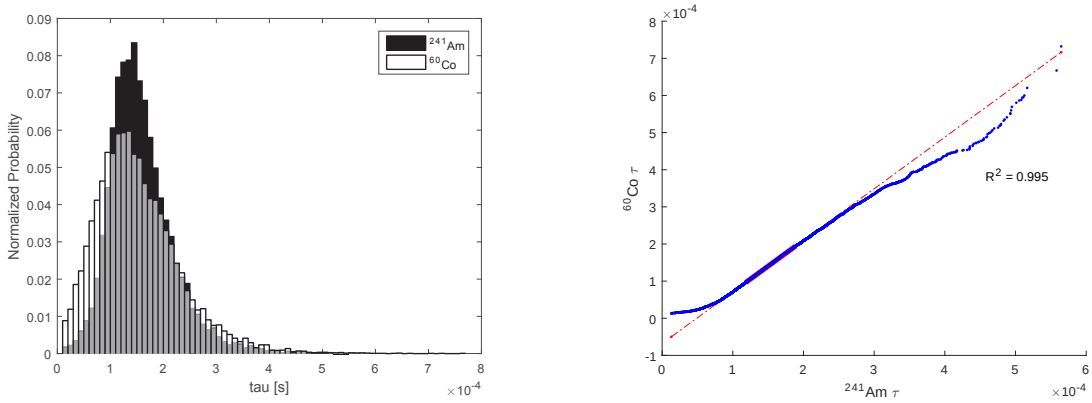

(a) (b)

Figure 35. Q-Q plot shortcomings. The τ probability distributions of ^{241}Am and ^{60}Co are plotted in (a). Visually these distributions are different and statistically the null hypothesis is rejected. However, the Q-Q plot (b) suggests they are the same.

Source Comparisons

Different sources were compared to each other. Figure 36 compares the τ distribution between sources. Generally, the ^{241}Am distribution is similar to the background distribution (Figure 36a). This could be due to the nature of the radiation. ^{241}Am and the UO_2 crystal have alpha particle decays. This could explain why the pulse decay times are similar. An alpha particle from ^{238}U decays with approximately 4.18 MeV; although an ^{241}Am alpha particle decays with approximately 5.48 MeV, it strikes the crystal with 4 MeV. These energies are remarkably similar and could result in the similarity between the two distributions. Figures 36b and 36c compare ^{241}Am to ^{60}Co and background to ^{60}Co respectively. The τ distributions are not similar.

In order to quantify the differences in the τ distribution, a Gaussian curve was fit to each distribution using the Gauss-Newton method. From the fit, a full width at half maximum (FWHM) was obtained. An example of an applied fit and the calculated FWHM is illustrated in Figure 37.

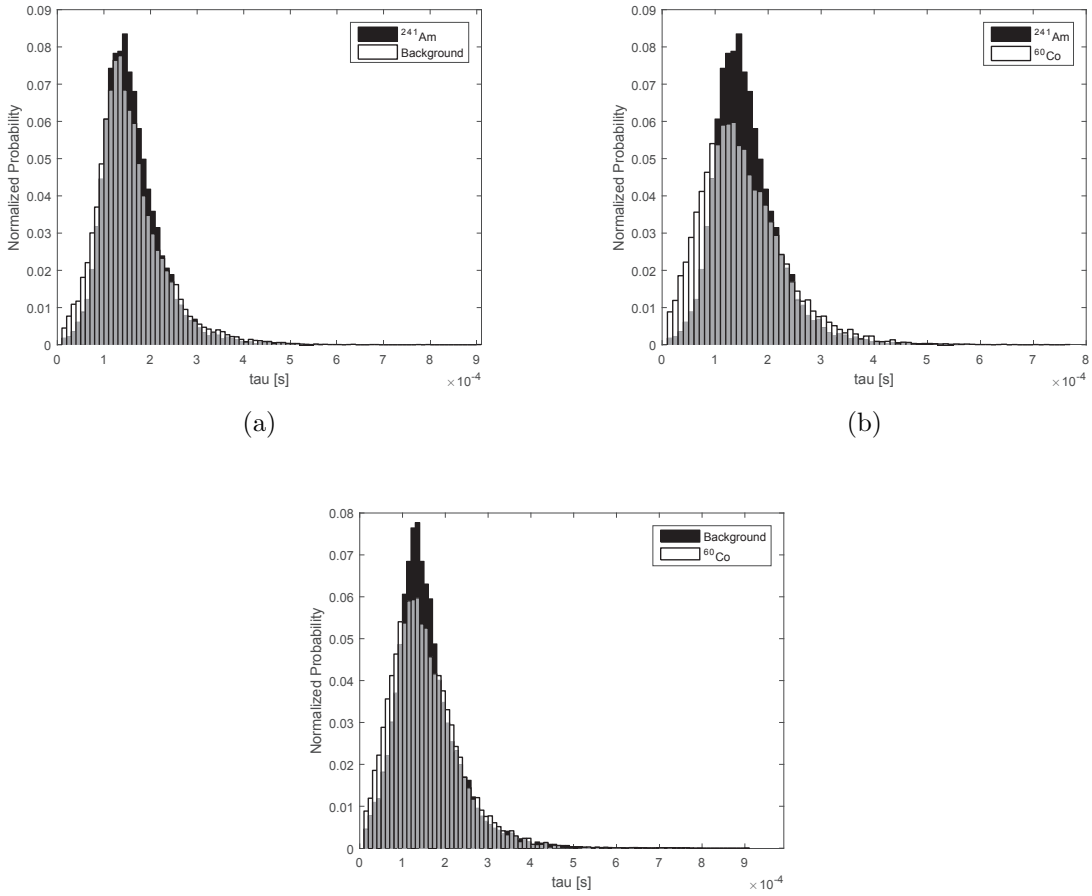

Figure 36. Comparison of τ probability distributions between sources. Figure (a) compares ^{241}Am to background. The τ distributions generally agree. Figure (b) compares ^{241}Am to ^{60}Co. Figure (c) compares background to ^{60}Co. The distributions compared in (b) and (c) are substantially different.

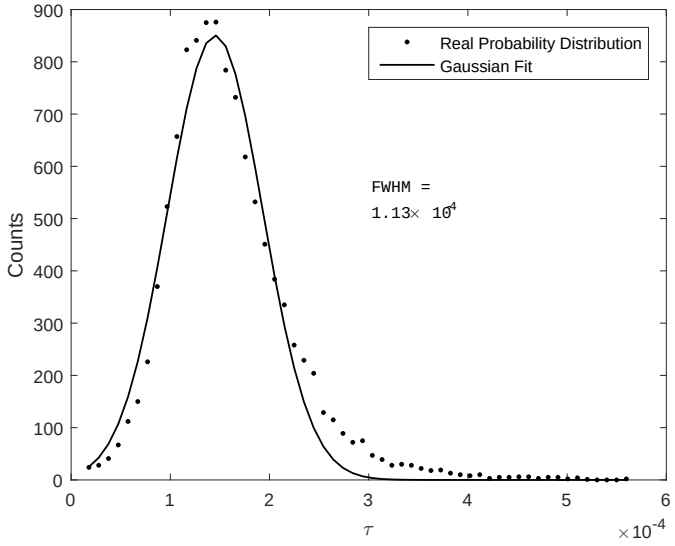

Figure 37. Example of a Gaussian fit applied to a τ distribution. From the fit, a FWHM can be obtained.

Each Gaussian fit has an associated error. Table 15 summarizes the result of the fit and the FWHM of the background, ^{241}Am, and ^{60}Co measurements from Figure 36. The error from each fit is primarily attributed to the fit along the tails and is assumed to contribute only negligibly to error in the FWHM.

Table 15. Summary of Gaussian fit and FWHM from measurements in experiment 6. The results of the calculated FWHM strongly suggest radiation may be separated based on the τ distribution.

Measurement	R^2	FWHM
Background 1	0.97	$1.26\times10^{-4}s$
Background 2	0.99	$1.24\times10^{-4}s$
^{241}Am 2	0.97	$1.13\times10^{-4}s$
^{60}Co 1	0.98	$1.69\times10^{-4}s$
^{60}Co 3	0.99	$1.67\times10^{-4}s$

From Table 15, the FWHM for ^{241}Am is approximately 10% less than that for background, and approximately 33% less than that for ^{60}Co. This evidence strongly suggests that the FWHM from the τ normalized probability distribution could be used to distinguish alpha particles from both background and high energy gammas.

4.4 Humidity Effects on Crystal Response

Prior to neutron irradiation, the crystal was kept in the laboratory under ambient conditions. Half of the experiment 2 data set were conducted inside the laboratory. The ^{60}Co and neutron experiments (from Table 9) were conducted in Edgewood, MD, inside a storage warehouse with no environmental controls. The humidity inside the building approached 100% while the temperature was between $40 - 75°$F. Environmental conditions were obtained daily from the National Weather Service and are summarized in Table 16. Due to the potential effect of humidity and temperature, the environmental conditions were monitored throughout and correlations were made with the collected data.

Table 16. Summary of weather conditions during neutron experiments. Neutron experiments were conducted inside of a warehouse with little insulation to the environment. The weather reports obtained from the National Weather Service were used to determine if environmental conditions affect the crystal's performance.

Date	Temperature Hi / Lo (Avg) [F]	Relative Humidity Hi / Lo (Avg)	Weather
OCT 26 2015	60/37 (49)	92/36 (64)	NSTR
OCT 27 2015	59/35 (47)	92/66 (79)	Light Rain
OCT 28 2015	70/54 (62)	100/86 (93)	Heavy Rain Fog
OCT 29 2015	70/47 (59)	100/37 (69)	Thunderstorms

Neutron Experiments

Warehouse Background Measurements

Prior to any irradiation, the background was measured. Although the crystal was not removed from the probe station during transport, the warehouse environment

was very different from other laboratory conditions. The background counting plot (Figure 38) was examined for any counting gaps or irregularities.

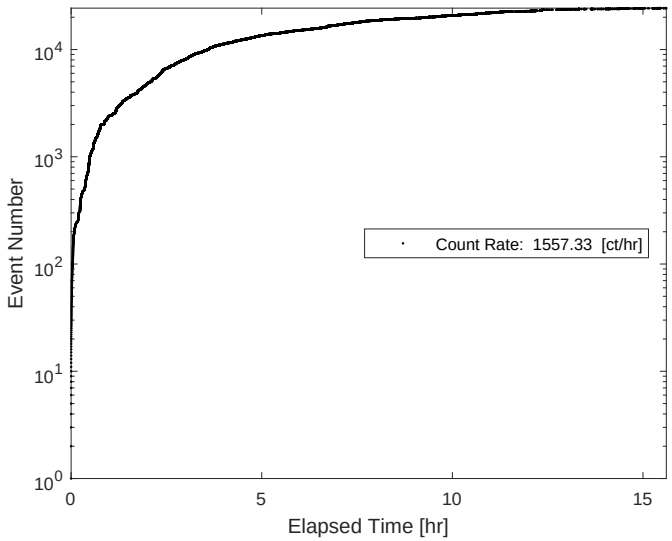

Figure 38. Background counting plot collected prior to neutron irradiation. From visual inspection, the plot has no major gaps indicating the crystal is responding as expected.

The counting plot was generally smooth and void of any serious gaps and the overall count rates were similar to previous experiments. Because of this, it was assumed the probes were in sufficient contact with the crystal. After background measurements were complete, neutron measurements were made.

Warehouse Neutron Measurements

Four separate neutron measurements were initially made and evaluated using the improved pulse analysis algorithm. The counting plot for the first measurement produced far too few expected counts, which was attributed to faulty wiring. The counting plots and V_{max}/τ histograms from the remaining three neutron measurements are presented below.

As plotted in Figure 39, it was observed that count rates were much higher than any previous laboratory measurement. This was expected since the ^{252}Cf source was

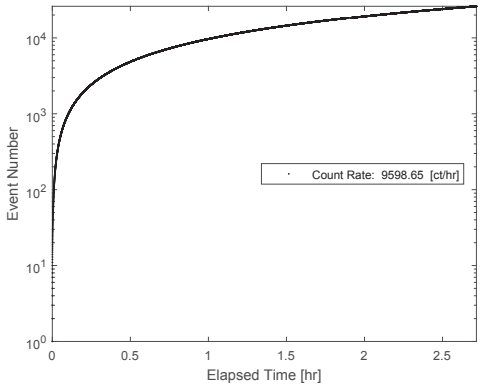

(a)

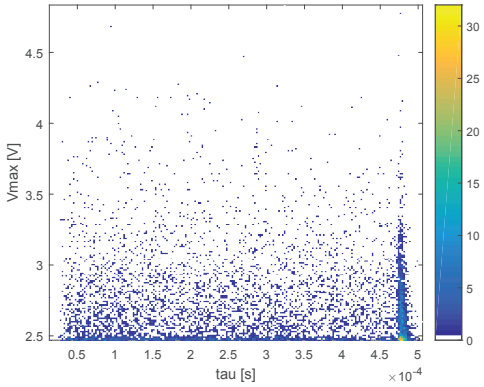

(b)

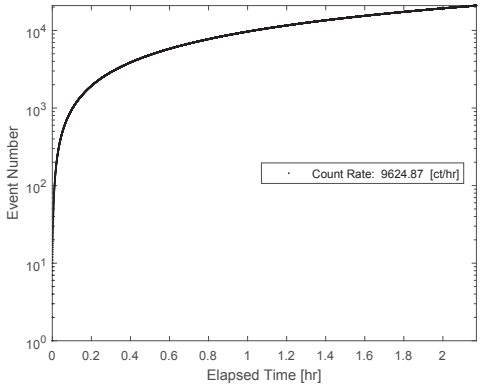

(c)

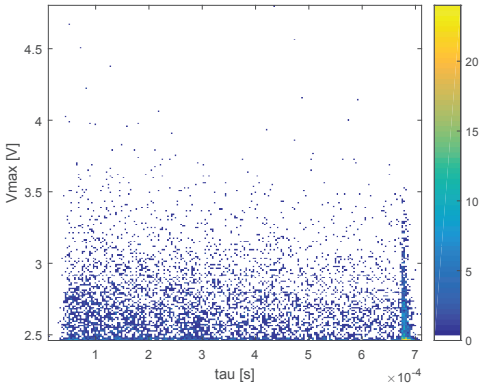

(d)

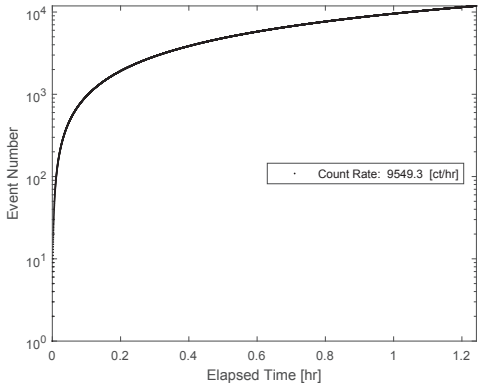

(e)

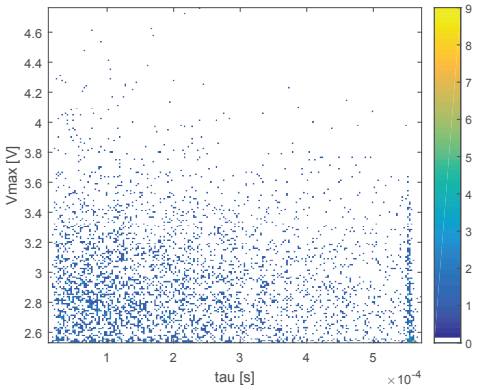

(f)

Figure 39. Counting plots and V_{max}/τ histograms from three neutron measurements. Count rates (>9,000 counts/hour) were much higher than any other previous measurements. At the time of data collection, the higher count rates were attributed to increased source activity.

an order of magnitude greater in activity than any previously used source ($\sim 10^7$ vs 10^6). However, the V_{max}/τ plots produced no distinct V_{max} or τ. This was likely due to environmental conditions. Inspection of the pulses resulted in a significant number of pulses being invalid. These invalid pulses were likely due to excessive surface leakage caused by the high humidity in the warehouse.

Adjusted Warehouse Background Measurements

After the first four neutron experiments were complete, a new background measurement was obtained to assess the effect of high humidity, which was 100% (Table 16). These measurements suggested a correlation between count rates, clipped pulses, and humidity. A chronological summary of each warehouse measurement and the subsequent laboratory measurements are presented in Table 17.

Table 17. Comparison of pulses from warehouse experiments and laboratory experiments. The experiments are listed in order data was collected.

Experiment	Measurement	Invalid Pulses	Clipped Pulses	Valid Pulses	Count Rate [ct/hr]
2	Background	7,925	2,193	14,195	1,557
	^{252}Cf	1,959	16,996	7,027	9,598
	^{252}Cf	2,790	10,672	7,440	9,624
	^{252}Cf	2,997	4,304	4,564	9,549
	Background	10,453	6,287	16,018	9,608
	^{252}Cf	5,431	1,196	3,474	9,122
	^{252}Cf	10,716	9,515	9,429	9,462
6	Background	16,929	1,313	14,432	1,515
	^{60}Co	17,023	1,474	14,270	5,205
	^{241}Am	13,521	6,996	12,250	9,408
	Background	16,341	2,249	14,177	1,208
	^{241}Am	16,108	1,294	10,945	406
	^{60}Co	16,048	1,473	14,886	8,520
	^{60}Co	17,205	1,508	14,008	4,236

Effects of Humidity on Count Rate

Table 17 indicates that with the exception of the first background measurement, all warehouse measurements have count rates exceeding 9,000 counts/hour. Two lab-

oratory measurements (discussed previously in section 4.3) have similar count rates. The warehouse measurements resulted in a hypothesis that humidity affects signal collection. In order to assess the effects of humidity, an experiment was conducted inside of a glove bag, which regulated humidity.

Figure 40 is a graphical representation of the count rates from all measurements recorded in the laboratory and glove bag. The relative humidity varied with ambient conditions. Relative humidity inside the glove bag was regulated to 48-52% and 15-22%.

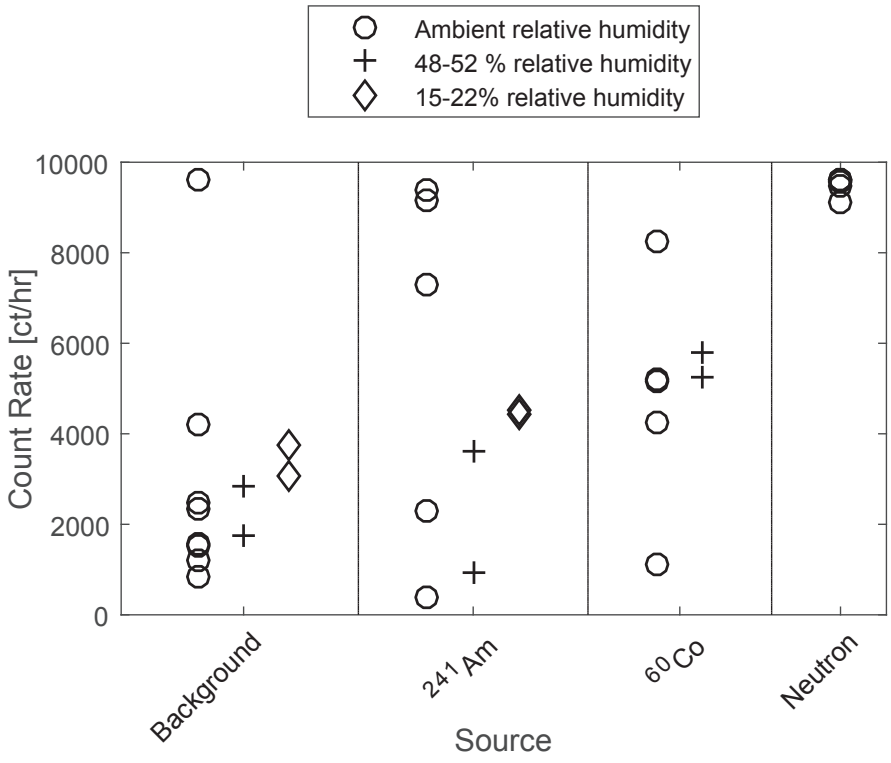

Figure 40. Comparison of count rates in different environments. Count rates above 9,000 ct/hr were not observed in humidity-controlled experiments.

In Figure 40, the count rates measured under 15-22% relative humidity appear to increase for each source. It is also observed that the data sets, overall, have less variation in count rates. While meaningful statistics cannot be obtained because the

number of experiments for each environment and source is extremely small, general patterns are observed. ^{60}Co measurements under dry conditions are not included because the crystal became dislodged.

In all experiments, the count rates in dry environments exceeded those measured in regulated humidity environments. This phenomenon indicates signal collection is being affected as humidity varies. The cause of the increased count rates is unknown, but appears to be related to the surface chemistry of the UO_2 crystal. Oxides are generally hydrophilic, and the removal of water vapor on the surface of the crystal may promote charge collection by the tungsten probes. However, excessive humidity ($\sim$ 100%) increases count rates. This could likely be caused from a combination of the leakage current and decreased resistivity from the water droplets on the crystal surface.

Effects of Humidity on Clipped Pulses

The effect of humidity on clipped pulses was examined by comparing the total number of clipped pulses in each type of environment. Figure 41 plots the number of clipped pulses for each source in each type of environment.

In general, a dry environment substantially reduced the number of clipped pulses:

- Background clipped pulses decreased from an average of 2,519 in ambient environments to 882 in dry environments (65% reduction).
- ^{241}Am clipped pulses decreased from an average of 5,728 in ambient environments to 678 in dry environments (89% reduction).

In addition to a reduction in clipped pulses, the dry environments also produced less variation in the number of clipped pulses, similarly observed in section 4.4.

The effect of humidity had the greatest impact on ^{241}Am experiments. This is largely because surface moisture on the crystal is yet another barrier the alpha particle

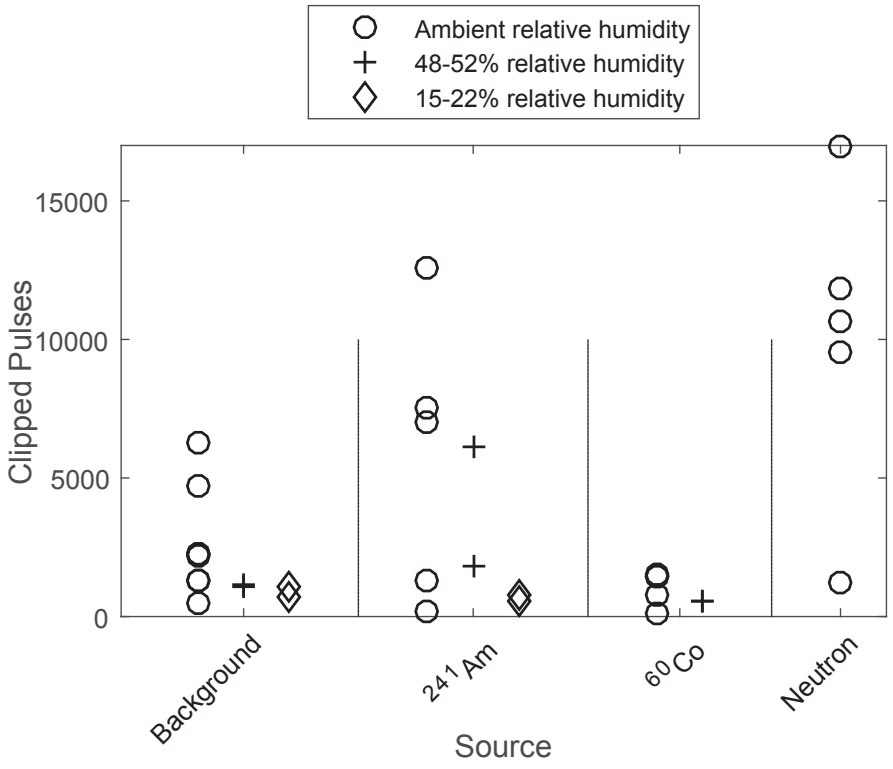

Figure 41. Comparison of clipped pulses in different environments.

must cross. Figure 42 plots the range and stopping power of an alpha particle in water. From Figure 42, an alpha particle will lose approximately 100 keV per micron when interacting with water. The result of decreasing the surface moisture is that the alpha particle strikes the crystal surface with greater energy than if water were present and can therefore penetrate further into the crystal.

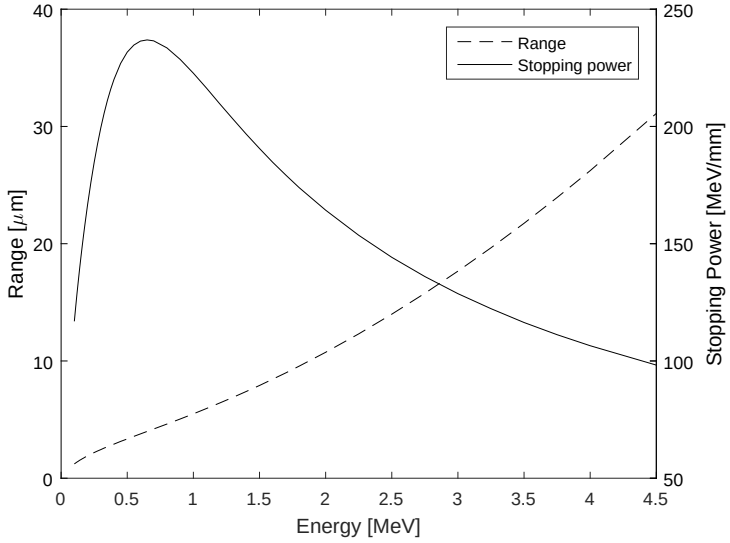

Figure 42. The range and stopping power of an alpha particle in water.

Effects of Humidity on τ

It has been established that τ distributions appear to vary between radiation sources. The effect of humidity on τ distributions was also examined. Background and dry ^{241}Am measurements from experiment 7(1) are plotted in Figure 43.

Unlike previous experiments, the background statistical comparisons are similar, such that the KS-test accepts the null hypothesis. The dry ^{241}Am experiments are different enough from each other, such that the KS-test rejects the null hypothesis on each comparison. Table 18 summarizes the FWHM of each measurement from experiment 7(1).

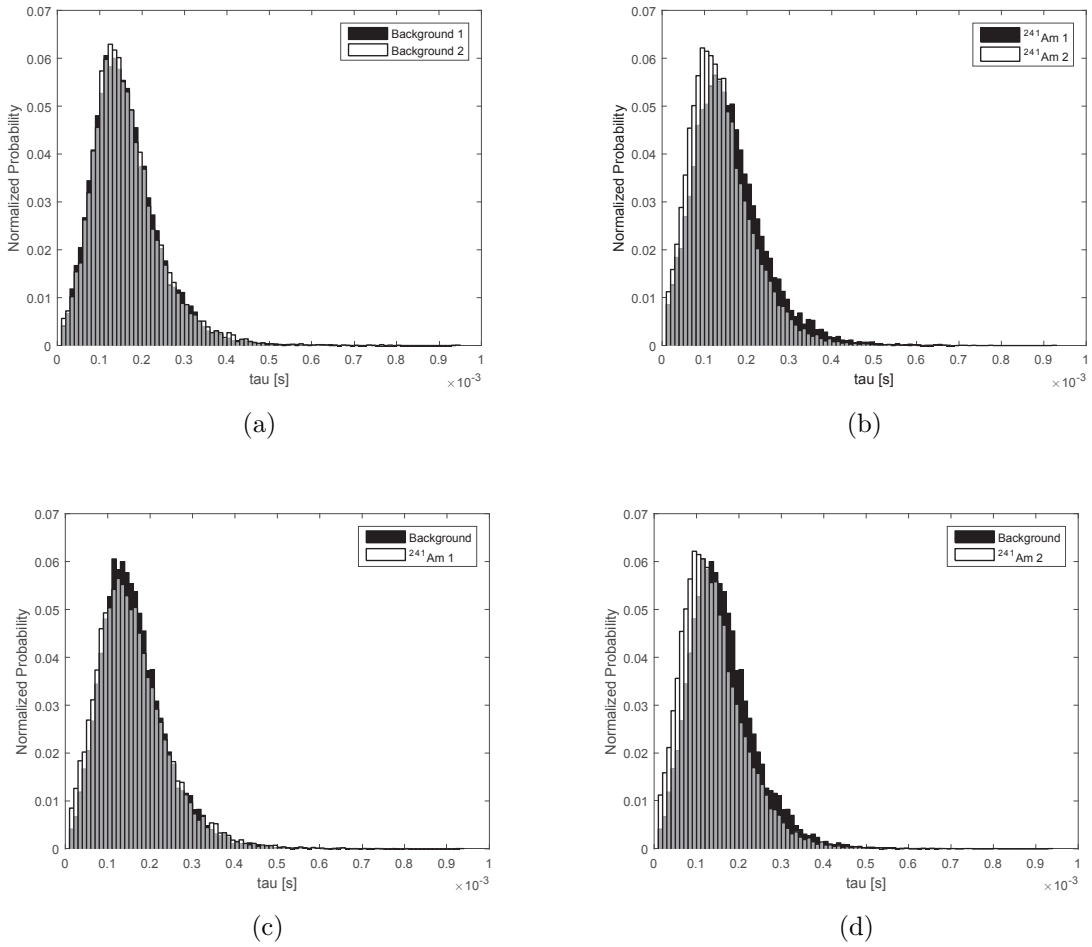

Figure 43. Comparison of τ probability distributions in a dry environment. Figure (a) compares backgrounds, (b) compares ^{241}Am, and (c) and (d) compare the background with an ^{241}Am measurement. The two background measurements are the only comparisons which result in the KS-test null hypothesis being accepted.

Table 18. Summary of Gaussian fit and FWHM from experiment 7(1) measurements. The background FWHM are, on average, approximately 8% less than the alpha particle FWHM.

Measurement	R^2	FWHM
Background 1	0.98	$1.58\times10^{-4}s$
Background 2	0.98	$1.52\times10^{-4}s$
^{241}Am	0.98	$1.76\times10^{-4}s$
^{241}Am	0.98	$1.61\times10^{-4}s$

From Table 18, variations in τ distributions between alpha particles and background measurements can be still separated. Unlike previous measurements (Table 15), the FWHM for ^{241}Am measurements are, on average 8% greater. This suggests it is still possible to separate radiation based on τ and supports the use of UO_2 as a radiation detector.

In order to assess how humidity affected the pulse decay times, comparisons between humid and dry τ were made. The probability distribution and cumulative distribution for background and ^{241}Am experiments are illustrated in Figure 44.

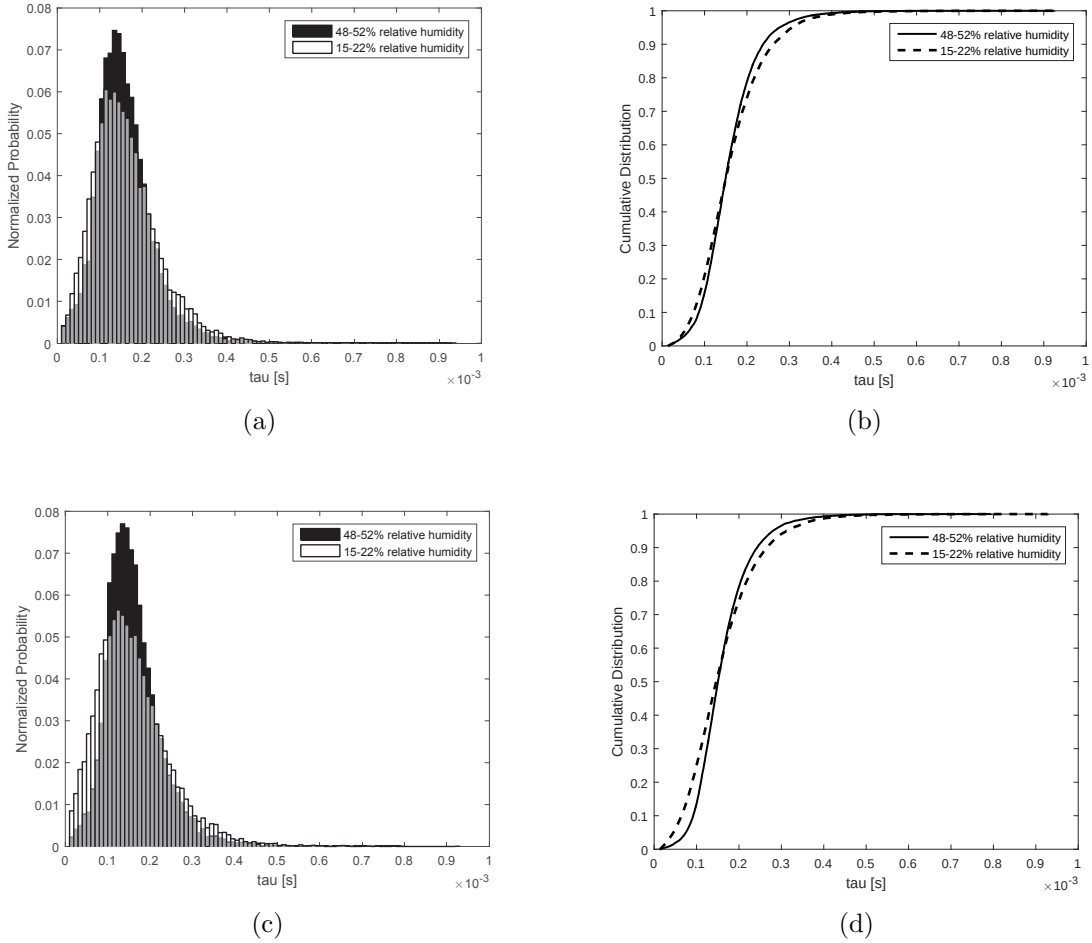

Figure 44. Comparison of τ distributions between environments. Figure (a) and (b) plot the background probability and cumulative distributions. Figure (c) and (d) plot the ^{241}Am probability and cumulative distributions. The KS-test rejects the null hypothesis for each comparison, indicating that although the sources are the same, the samples are different.

The cumulative distribution plots highlight the sensitivity of the KS-test. Although visually similar, the KS-test rejects the null hypothesis for each experiment, indicating these distributions are different. Based on the probability distributions in Figure 44, the overall effect of humidity is to reduce variation in τ. This is confirmed in Table 19, which compares the FWHM of measurements in experiment 7(1) to 7(2).

Table 19. Comparison of Gaussian fit and FWHM between experiments 7(1) and 7(2) measurements. The overall effect of humidity is to narrow the τ distribution resulting in a reduction in the FWHM.

Measurement	R^2	FWHM 7(1)	FHWM 7(2)
Background 1	0.98	$1.58\times10^{-4}s$	$1.28\times10^{-4}s$
Background 2	0.98	$1.52\times10^{-4}s$	$1.47\times10^{-4}s$
^{241}Am 1	0.98	$1.76\times10^{-4}s$	$1.18\times10^{-4}s$
^{241}Am 2	0.98	$1.61\times10^{-4}s$	$1.44\times10^{-4}s$

The reason for this reduction in τ variability is unknown. Regardless of environmental conditions, it is still possible to discriminate radiation from background, which further suggests that radiation can be separated based upon pulse decay times.

4.5 Adjusted Effects of Humidity on Crystal Response

Because the crystal became dislodged during experiment 7, a new experiment with new probe locations was conducted. Background, ^{241}Am, and ^{60}Co measurements were recorded under two relative humidity conditions: dry (15-22% relative humidity) and humid (80-90% relative humidity). Figure 45 compares like-measurements and Figure 46 compares measurements between sources. Both data sets were from experiment 8(1). In each figure, the normalized probability distributions are presented alongside the cumulative distribution plots for each measurement.

The CDF plots in Figure 45 suggest that measurements among like-sources are essentially identical. However, in Figure 46, variability in data is minimal. Although the KS-test rejects τ distributions between background and radiation sources, the test

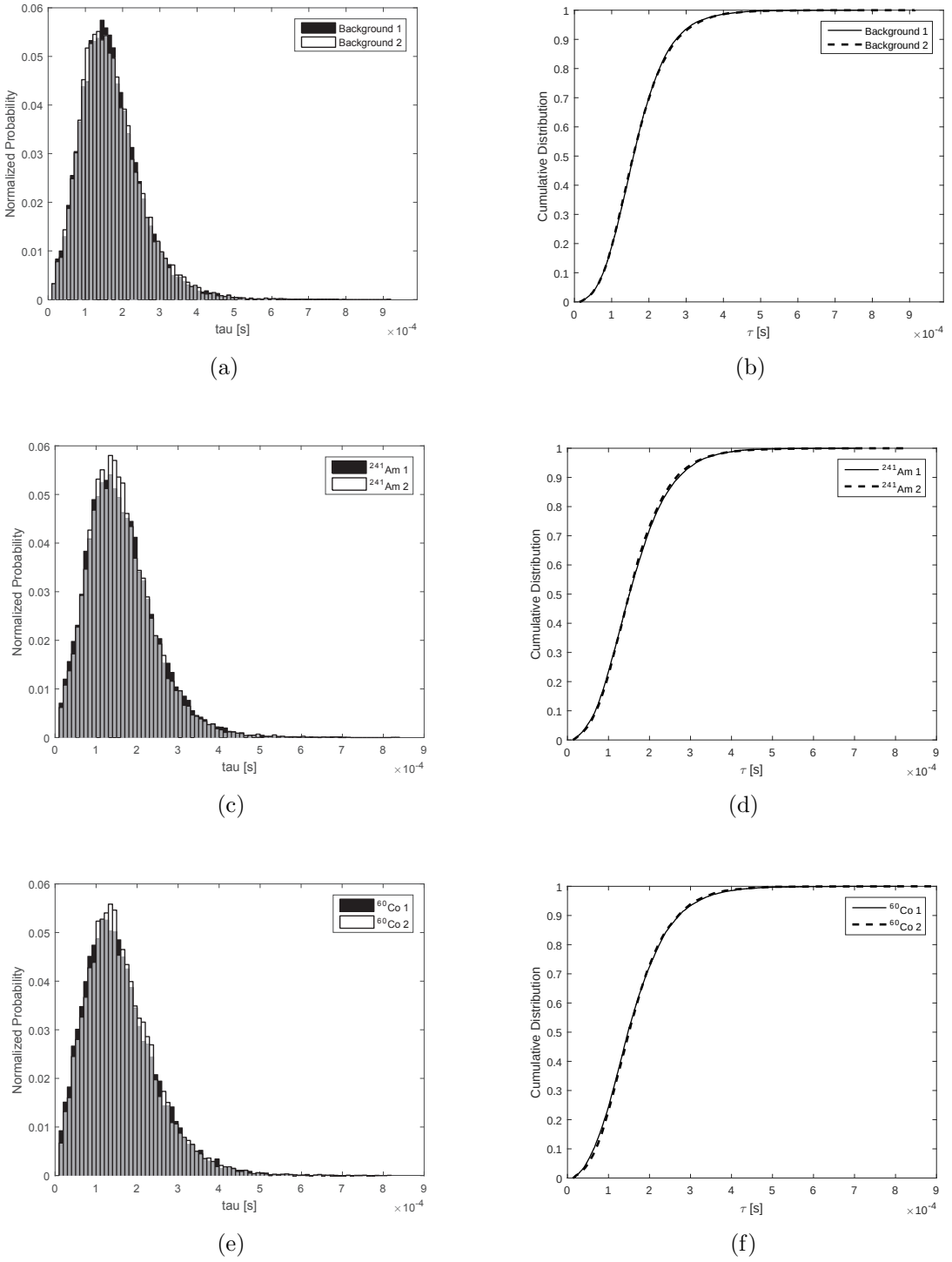

Figure 45. Comparison of τ distributions between like-measurements. Figures on the left compare the normalized probability distributions and figures on the right compare the cumulative distributions for (a–b) background, (c–d) ^{241}Am, (e–f) ^{60}Co.

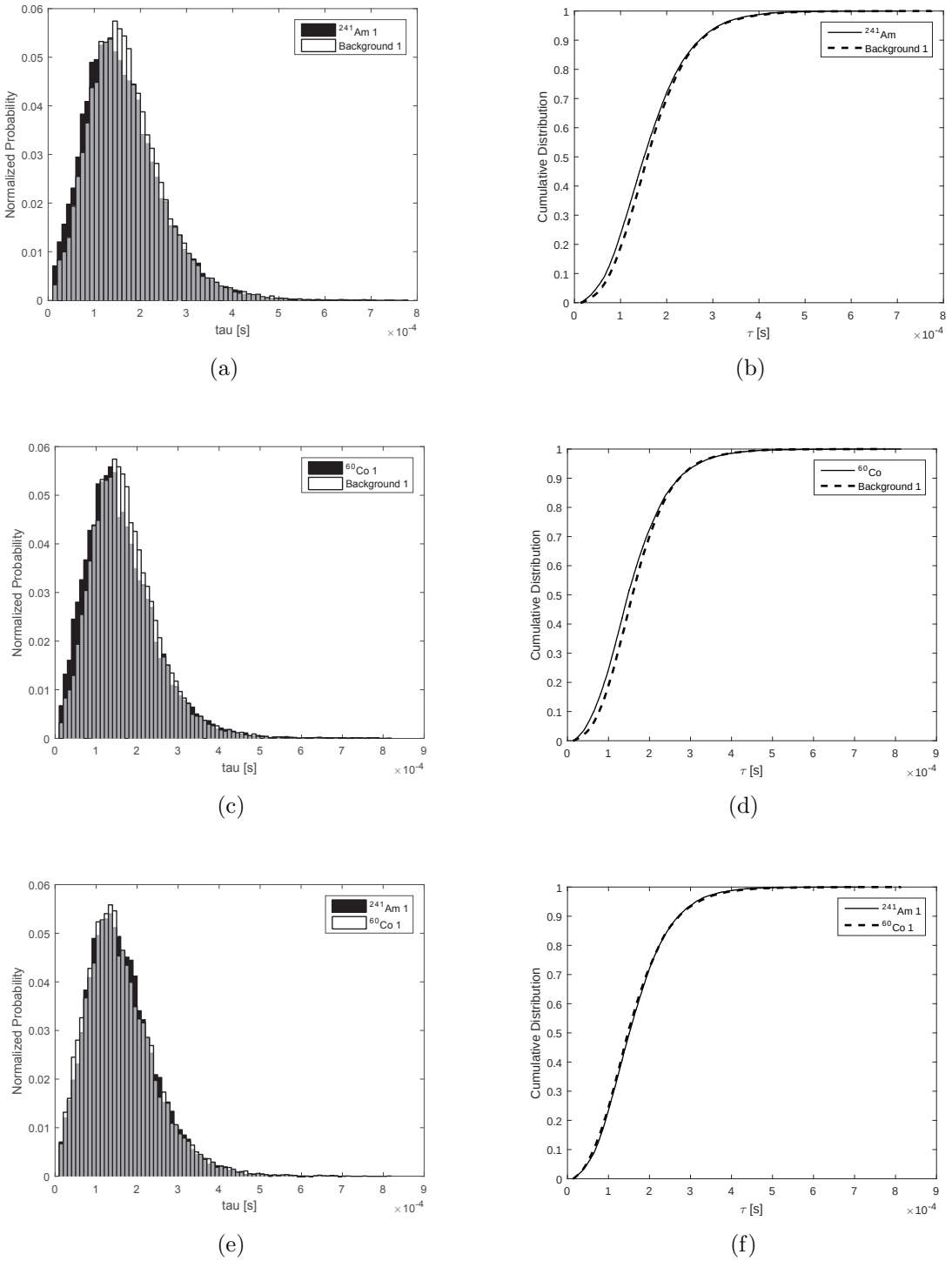

Figure 46. Comparison of τ distributions between (a–b) background and ^{241}Am, (c –d) ^{60}Co and background, (e–f) ^{241}Am and ^{60}Co.

accepts the null hypothesis when comparing radiation sources. This indicates that while radiation can be separated from background, determining the type of radiation is not possible. Differences in τ distributions were expected but not observed. These results further support the conclusion that the response from the crystal is extremely sensitive to contact probe location.

Table 20. Summary of Gaussian fit and FWHM from experiment 8(1) measurements. With new probe contact locations, the ability to separate radiation based on τ is no longer possible.

Measurement	R^2	FWHM
Background 1	0.99	$1.69\times10^{-4}s$
Background 2	0.98	$1.70\times10^{-4}s$
^{241}Am 1	0.98	$1.83\times10^{-4}s$
^{241}Am 2	0.98	$1.70\times10^{-4}s$
^{60}Co 1	0.98	$1.85\times10^{-4}s$
^{60}Co 2	0.98	$1.73\times10^{-4}s$

Pulses collected under experiment 8(2) were similar to neutron measurements and were mostly invalid. However, this experiment confirmed the general correlation between high humidity and increased number of clipped pulses.

Neutron Detection

Neutron detection was not demonstrated. Pulses resulting from the neutron measurements were largely invalid, containing a large amount of clipped pulses. This was attributed to high humidity and weather conditions, but the exact cause could not be attributed to one variable.

5. Conclusions

5.1 Primary Conclusions of Research

The aim of this research was to detect fast neutrons using a novel, single-crystalline UO_2 sample. Based on current data and experimental design, it is not determined whether neutrons can be detected. This is due to the crystal being exceptionally sensitive to contact placement. Data collected at one contact location can only be compared to other data from the same location.

The pulse decay analysis suggests that different types of ionizing radiation may be separable. Gamma irradiation from ^{60}Co appear to have longer decays than alpha irradiation from ^{241}Am. The KS-test was used to determine whether the decay distributions were similar. The null hypothesis (distributions are the same) was rejected when different sources (^{241}Am and ^{60}Co) were compared. The null hypothesis was accepted when comparing like-measurements. This is encouraging.

Experiments in which humidity was controlled suggest a requirement to control humidity to obtain valid pulses. Humidity also affected τ distributions, which were consistently broader in low humidity. The calculated FWHM for background and ^{241}Am distributions were respectively increased, on average, by 12% and 33%.
τ distributions are still unique to each source and results from the KS-test suggest it is still possible to separate alpha radiation from gamma radiation as long as the comparisons are in the same environmental conditions.

^{252}Cf measurements were inconclusive because of the effects of high humidity. Collected pulses were largely clipped and invalid. Future experiments with ^{252}Cf should be conducted under dry conditions.

5.2 Significance of Research

A method, based on pulse shape discrimination and pulse decay time, has been developed with some success. By analyzing the pulse decay distributions, it is possible to distinguish between background, alpha, and high-energy gamma radiation with a fair degree of certainty on the crude system. Based on this method, neutron detection may also be possible. This research used this method for analyzing UO_2 irradiation. Because single-crystalline UO_2 is a novel material, this work has significantly advanced the scientific knowledge in its use as a radiation detector.

5.3 Recommendations for Future Research

Single-crystalline UO_2 is a novel material and has been shown to function as a primitive radiation detector. Future research will improve its efficiency as a detector. Charge collection is currently inefficient and highly based on contact probe location. In order to efficiently detect charge resulting from a radiation interaction, electrical contacts must be added to the crystal. AFRL has recently grown a substantially larger crystal. A larger crystal would facilitate research with electrical contacts and thereby reduce variability based upon uncontrollable contact parameters.

The $\mu\tau$-product is an indicator of how well a material will perform as a semiconductor. However, information regarding charge carriers within single-crystalline UO_2 is non-existent. Future research, such as Hall measurements, could provide valuable insight into the semiconductor properties of single-crystalline UO_2 once contacts can be consistently made.

The ultimate goal of this research was to detect fast neutrons without a conversion layer. These experiments failed to provide evidence to conclude neutron detection. For future measurements, a higher neutron-energy source is recommended. While ^{252}Cf emits fast neutrons, the average neutron energy is approximately 1 MeV. At

this energy, the fission cross section for ^{238}U is less than 1 barn. However, the fission cross section increases with increasing neutron energy. It may be desirable to perform neutron experiments with higher-energy neutron sources as from a neutron generator or PuBe source.

Bibliography

1. T. Feder, "US Government Agencies Work to Minimize Damage Due to Helium-3 Shortfall," *Physics Today*, vol. 62, pp. 21–23, 2009.

2. A. Cho, "Helium-3 Shortage Could Put Freeze on Low-Temperature Research," *Science*, vol. 326, pp. 778–779, 2009.

3. L. J. Wittenberg, "Non-Lunar Helium-3 Resources," in *Second Wisconsin Symposium On Helium-3 and Fusion Power*, 1994, p. 11.

4. J. Mann, September 2015, private communication.

5. T. Meek *et al.*, "Semiconductive Properties of Uranium Oxides," in *Waste Management 2001 Symposium*, 2000.

6. C. A. Kruschwitz *et al.*, "Semiconductor Neutron Detectors using Depleted Uranium Oxide," in *Hard X-Ray, Gamma-Ray, and Neutron Detector Physics XVI*, 2014.

7. T. T. Meek and B. von Roedern, "Semiconductor Devices Fabricated from Actinide Oxides," *Vacuum*, vol. 83, pp. 225–228, 2009.

8. K. S. Krane, Ed., *Introductory Nuclear Physics*, 3rd ed. Hoboken, NJ: Wiley, 1987.

9. N. J. Carron, *An Introduction to the Passage of Energetic Particles through Matter*, 1st ed. Abingdon, UK: Taylor & Francis, 2006.

10. "Evaluated Nuclear Data File (ENDF)," https://www-nds.iaea.org/exfor/endf.html.

11. G. F. Knoll, *Radiation Detection And Measurement*, 4th ed. Hoboken, NJ: Wiley, 2010.

12. P. Peerani *et al.*, "Testing on Novel Neutron Detectors as Alternative to He-3 for Security Applications," *Nuclear Instruments and Methods in Physics Research A*, vol. 696, pp. 110–120, 2012.

13. R. T. Kouzes *et al.*, "Progess in Alternative Neutron Detection To Address the helium-3 Shortage," *Nuclear Instruments and Methods in Physics Research A*, vol. 784, pp. 172–175, 2015.

14. A. J. Peurrung, "Recent Developments in Neutron Detection," *Nuclear Instruments and Methods in Physics Research A*, vol. 443, pp. 400–415, 1999.

15. C. Jammes *et al.*, "Neutron Flux Monitoring System of the French GEN-IV SFR," *Nuclear Engineering and Design*, vol. 270, pp. 273–282, 2014.

16. S. M. Sze, *Physics of Semiconductor Devices*, 3rd ed. Hoboken, NJ: Wiley, 1985.

17. C. Petrillo *et al.*, "Solid State Neutron Detectors," *Nuclear Instruments and Methods in Physics Research A*, vol. 378, pp. 541–551, 1996.

18. D. S. McGregor *et al.*, "Present Status of Microstructured Semiconductor Neutron Detectors," *Journal of Crystal Growth*, vol. 379, pp. 99–110, 2013.

19. C. J. Bridgman, *Introduction to the Physics of Nuclear Weapons Effects*. Fort Belvoir, VA: Defense Threat Reduction Agency, 2001.

20. J. K. Shultis and R. E. Faw, *Fundamentals of Nuclear Science and Engineering*. Boca Raton, FL: CRC Press, 2008.

21. G. V. Samsonov, *The Oxide Handbook*. New York, NY: IFI/Plenum Data Company, 1982.

22. S. Francis *et al.*, "Uranium Dioxide Semiconductor Neutron Detector," 2010, unpublished.

23. L. R. Morss *et al.*, Eds., *The Chemistry of the Actinide and Transactinide Elements*, 4th ed. Dordrecht, The Netherlands: Springer, 2010.

24. C. Young *et al.*, "Novel Radiation Detection with UO2 Single Crystals," Air Force Institute of Technology, 2015.

25. "Chart of Nuclides," http://www.nndc.bnl.gov/chart/.

26. J. F. Ziegler *et al.*, *SRIM - The Stopping And Range of Ions in Matter*. Morrisville, NC: Lulu Press, 2008.

27. T. Herold, "Energy Spectra of Neutrons and Gamma Rays from Spontaneous Fission of Cm-244," AEC Research and Development Report, 1965.

28. J. A. Peacock, "Two-dimensional goodness-of-fit testing in astronomy," *Monthly Notices of the Royal Astronomical Society*, vol. 202, no. 3, pp. 615–627, 1983.

29. D. Muir, "Two-dimensional (2D) paired Kolmogorov-Smirnov test - File Exchange - MATLAB Central," http://www.mathworks.com/matlabcentral/fileexchange/38617-two-dimensional--2d--paired-kolmogorov-smirnov-test, 2013.

Vita

MAJ Stephan Varga graduated from North Georgia College & State University with a Bachelor's Degree in Chemistry and was commissioned as 2LT in the US Army Chemical Corps in 2003. He has served in variety of positions at the unit level to include platoon leader, executive officer, company commander and technical escort team leader. During this time, he deployed twice to Iraq. In 2010, MAJ Varga was awarded a Master's Degree in Environmental Management from Webster University. In 2011, MAJ Varga transitioned to Functional Area 52. His most recent assignment was serving as a Characterization Team Leader in a Nuclear Disablement Team.

REPORT DOCUMENTATION PAGE

Form Approved
OMB No. 0704–0188

1. REPORT DATE *(DD–MM–YYYY)*	2. REPORT TYPE	3. DATES COVERED *(From — To)*
24–03–2016	Master's Thesis	June 2014 - March 2016

4. TITLE AND SUBTITLE

Radiation Response from a Novel UO_2 Crystal

5a. CONTRACT NUMBER

5b. GRANT NUMBER

5c. PROGRAM ELEMENT NUMBER

6. AUTHOR(S)

Varga, Stephan A., MAJ, USA

5d. PROJECT NUMBER

5e. TASK NUMBER

5f. WORK UNIT NUMBER

7. PERFORMING ORGANIZATION NAME(S) AND ADDRESS(ES)

Air Force Institute of Technology
Graduate School of Engineering and Management (AFIT/EN)
2950 Hobson Way
WPAFB OH 45433-7765

8. PERFORMING ORGANIZATION REPORT NUMBER

AFIT-ENP-MS-16-MS-084

9. SPONSORING / MONITORING AGENCY NAME(S) AND ADDRESS(ES)

Domestic Nuclear Detection Office
Samantha Connelly
245 Murray Ln SW #0115
Washington DC 20528
samantha.connelly@dhs.gov

10. SPONSOR/MONITOR'S ACRONYM(S)

DNDO

11. SPONSOR/MONITOR'S REPORT NUMBER(S)

12. DISTRIBUTION / AVAILABILITY STATEMENT

Distribution Statement A. Approved for public release; Distribution Unlimited.

13. SUPPLEMENTARY NOTES

This material is declared work of the U.S. Government and is not subject to copyright protection in the United States.

14. ABSTRACT

The radiation response of a novel, single-crystalline UO_2 sample was analyzed using several types of radiation. The crystal was exposed to alpha, gamma, and neutron radiation under various environmental conditions and the electronic response of the crystal was measured using a pulse shape discrimination algorithm. The distributions of pulse amplitude (V_{max}) and pulse decay times (τ) were used to compare the output.

This research revealed that the crystal radiation response is exceptionally sensitive to surface conditions, specifically humidity, which tends to alter the time dependent currents resulting from the radiation interactions. The pulse τ can be made to be uniquely distributed for a certain set of conditions allowing to discern alpha, background and gamma irradiation, but it cannot be consistently reproduced. The overall $\Delta\tau$ itself was uniform for all radiation sources measured and the decay distributions were statistically different. This suggests that with well controlled environments, τ distributions may be sufficient to identifying a radiation interaction type.

This preliminary research on novel uranium-based detectors indicates that further research into the crystal surface electronic structure is needed if it is possible to separate radiation types, especially neutron interactions. Furthermore, developing a better method for making crystal contacts to ensure bulk conductivity is a priority.

15. SUBJECT TERMS

UO_2, Neutron detection, Radiation response

16. SECURITY CLASSIFICATION OF:			17. LIMITATION OF ABSTRACT	18. NUMBER OF PAGES	19a. NAME OF RESPONSIBLE PERSON
a. REPORT	b. ABSTRACT	c. THIS PAGE			James C. Petrosky, AFIT/ENP
U	U	U	UU	96	19b. TELEPHONE NUMBER *(include area code)* (937)255-3636 x.1234; james.petrosky@afit.edu